Available online at www.sciencedirect.com
ScienceDirect
Comput. Methods Appl. Mech. Engrg. 389 (2022) 114394
Computer methods in applied mechanics and engineering
www.elsevier.com/locate/cma

Conformal topology optimization of multi-material ferromagnetic soft active structures using an extended level set method

Jiawei Tian[a], Manqi Li[b], Zhonghao Han[b], Yong Chen[b], Xianfeng David Gu[c,d], Q.J. Ge[a], Shikui Chen[a,*]

[a] *Department of Mechanical Engineering, State University of New York, Stony Brook, NY, 11794, USA*
[b] *Department of Aerospace and Mechanical Engineering, University of Southern California, Los Angeles, CA, 90089, USA*
[c] *Department of Computer Science, State University of New York, Stony Brook, NY, 11794, USA*
[d] *Department of Applied Mathematics and Statistics, State University of New York, Stony Brook, NY, 11794, USA*

Received 17 July 2021; received in revised form 11 October 2021; accepted 22 November 2021
Available online xxxx

Abstract

Ferromagnetic soft active structures using embedded ferromagnetic particles in the soft polymer matrix can generate flexible locomotion and change configurations remotely, rapidly, and biologically friendly with an applied magnetic field. To achieve the desired motion, these soft active structures can be designed by tailoring the layouts of the ferromagnetic soft polymer. Although many magnetic soft active structures have been designed and fabricated, they are limited by the developer's intuition and experience. Structural topology optimization has become a promising method to achieve innovative structures by optimizing the material layout, opening a new path for architecting ferromagnetic-driven active structures. Given the widespread adoption of thin-shell structures for soft robots, the extended level set method (X-LSM) and conformal geometry theory are employed to perform topology optimization of the ferromagnetic soft active structures on manifolds. The boundary evolution on a free-form 3D surface can be transferred into a 2D rectangular plane by solving a modified Hamilton–Jacobi equation weighted by conformal factors. The reconciled level set (RLS) method is firstly implemented within the X-LSM framework in this paper to enable the design of multi-material ferromagnetic soft active structures on free-from surfaces. The design objective consists of a subobjective function for kinematic requirement and a subobjective function for minimum compliance. The shape sensitivity was analyzed using the material time derivative and the adjoint variable approach. The proposed method was applied to design several single and multi-material ferromagnetic soft active structures. Two topologically optimized designs have been printed using functional 3D printing technology, or the so-called 4D printing, to physically realize soft active structures with built-in functionalities. The results of the numerical verification and experimental validation demonstrate the effectiveness of the proposed design and fabrication framework.

Keywords: Multimaterial conformal topology optimization; Soft active structures; Extended level set method; Conformal geometry theory; Design-dependent topology optimization; Functional 3D printing

* Corresponding author.
E-mail address: Shikui.Chen@stonybrook.edu (S. Chen).

https://doi.org/10.1016/j.cma.2021.114394
0045-7825/

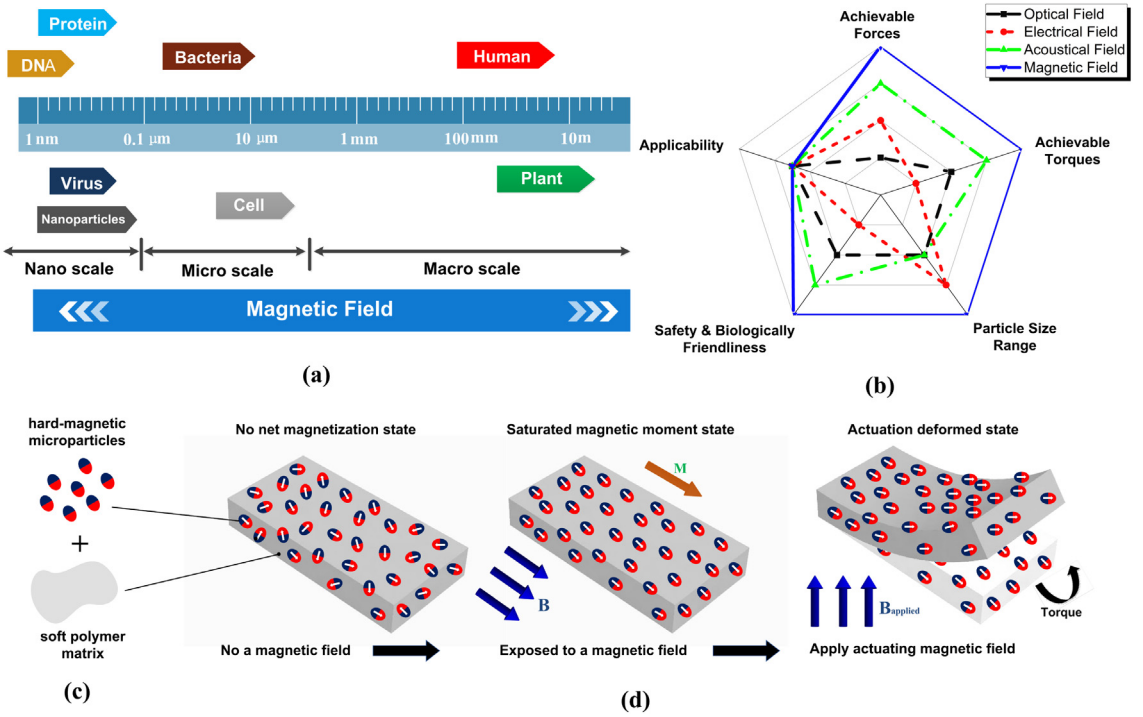

Fig. 1. (a) The application of magnetic manipulation for various size scales of objects. (b) A comparison of different actuation strategies of soft active materials. (c) The composition of the hard-magnetic polymer. (d) A schematic beam model for illustrating the magnetic torque. (For interpretation of the references to color in this figure legend, the reader is referred to the web version of this article.)

1. Introduction

1.1. Magnetic soft active structures: State of the art

In response to an external stimulus, soft active materials (SAM) can generate desired movements through shape shifting, ranging from simple bending, folding, or twisting to more complex transformations. Hence, they have recently received growing attention in a plethora of tantalizing engineering applications, such as soft robots [1,2], compliant electronics [3,4], and bionic medical devices [5,6]. Unlike their rigid-body counterparts, where motion is caused by the relative position change of rigid components, the SAM enabled soft active structures can generate flexible motions through large deformations of soft materials [7].

Numerous external fields have been used to control soft active matters, including the magnetic field [8], electric field [9], acoustic field [10], and optical field [11]. The optical field tends to induce local overheating and requires a transparent optical environment, limiting its applicability [12,13]. The electric field may cause safety problems as the electrochemical reaction inside the soft matter is inevitable [13,14]. The acoustic field can only provide a relatively small force, and the scale of the particles it can control is particularly limited [13]. Among such manipulation strategies, magnetic stimulation offers many notable benefits. First, among these manipulation strategies, the magnetic field can generate the highest forces and torques, which enable it to control both macroscopic objects and microscopic structures to manipulate particles such as cells, viruses, bacteria, and even nanoparticles, shown in Fig. 1(a) [13,15,16]. Second, because the magnetic field allows fast and contactless control, it is considered as a safe and biologically friendly interaction approach [17]. In summary, the different manipulation strategies are compared using a radar chart in Fig. 1(b), where the blue line represents the magnetic field.

The shape alternations of ferromagnetic soft polymer are achieved by shaping ferromagnetic particles in the matrix of soft polymer. The typical composition of the ferromagnetic polymer is illustrated in Fig. 1(c). As shown in Fig. 1(d), ferromagnetic particles are initially randomly distributed in the polymer matrix of the beam after printing. Therefore, there is no net magnetization along the beam. The overall magnetic moment along the axis

direction can be tuned by exposing the ferromagnetic beam to a strong magnetic field B. Under the actuation of the external actuating magnetic field, a magnetic torque acts on the magnetized soft material and forces it to bend towards a new configuration. Consequently, the direction of the inner magnetization vector in the soft material has a tendency to be parallel to the external magnetic flux. Most soft robots using magnetic hard magnetic particles are attained by leveraging this physical property. Recently, Xu et al. [17] fabricated flexible magnetic planar structures by patterning hard magnetic particles in a matrix of soft polymer cured by ultraviolet lithography. Wu et al. [18] have designed a series of 2D magnetically actuated metamaterial systems which can obtain tunable mechanical properties, including negative Poisson's ratio, buckling, and tailorable stiffness. Kim, Zhao and Wang et al. [8,19,20] proposed a fabrication technique by applying an external magnetic field to the dispensing nozzle to reorient the hard magnetic particles during the printing process, with which the resultant designs can produce programmed morphology and motion between planar structures and complex 3D structures. Lum [21] investigated this subject and proposed a programming method to automatically calculate the magnetization and magnetic field required for soft magnetic materials to achieve the desired shapes. Interestingly, all the existing work has focused on the soft robots using hard magnetic particles like ferromagnetic particles, which can hold the remnant magnetization even if the applied magnetic field is removed [19]. The remnant magnetization of hard magnetic particles enables a complex and convoluted shape change [17,22,23].

While these flexible magnetism-sensitive robots are well constructed to achieve the desired motions and functions, several limitations exist. First of all, all the soft polymer matrix shapes where the magnetic particles are patterned are planar in 2D. There is no matrix shape based on free-form surfaces, which is common in industrial applications [24], including flexible electronics [25,26], aircraft, and aerospace structures [27–29]. The stiffness of these designed structures has not been taken into account, making the design inaccessible since soft robots have to resist the reaction force when touching objects. Most importantly, all of these designs, to a large extent, are the product of intuitions, experiences, and bioinspiration [30]. A systematic design method for magnetically driven soft robots is still in its infancy and is somewhat underdeveloped. To overcome these limitations, a new design method is needed to create those 'soft machines' to realize the specific functions of the applications, which will enhance the latent versatility of soft robots.

1.2. Designing soft robot using topology optimization

Topology optimization (TO) can find an optimal layout of material in a design domain to attain the desired structural performance. TO was originally proposed to optimize lightweight structures, which have lately been extended to various problems with multiphysics coupling features, such as electromagnetics, thermomechanics, fluidics, or acoustics, et al. [31–35].

Topology optimization as a promising methodology for designing soft robots remains under-exploited. Recently, Behrou et al. [36] employed an element removal strategy into the design of a force inverter compliant mechanism, which achieves remarkable computational savings. Wu et al. [37] designed a metamaterial mechanisms using the density-based method combined with a variable linking scheme. Geiss et al. [38] designed a 4D printed heat-activating structure to produce a large displacement using the level set method and the density-based method. Chen et al. [39] designed a soft gripper actuated by cables in the form of a concentrated load based on the level set method. Furuta et al. [40] designed a Peltier effect thermoelectric actuator to achieve the maximum transduction energy using the level set method. Earlier contribution by Wang and Chen et al. [41] proposed a level-set-based framework to design compliant mechanisms capable of transmitting motion from the input port to the output port. In those works, most of the designs were driven by traditional contact force or pressure. Few studies have investigated non-contact actuation such as the magnetic stimulation throughout the volume of the geometry. Topology optimization of magnetic actuators has also been examined in the past decade. Park et al. [42,43] designed a lighter magnetic actuator with maximal magnetic energy using the level-set-based topology optimization. Ryu and Park et al. [44,45] also employed the level set method to design a magnetic actuator, which can achieve the maximum actuating force with limited usage of ferromagnetic material. Also, Li et al. [46] proposed a toolkit to design an electromagnetic actuator to achieve maximal magnetic force based on genetic algorithm and differential evolutionary algorithm. However, these studies were mainly concerned with the optimization of magnetic energy or magnetic force rather than kinematic performance.

Geometry and material, two perpetual themes in soft robot design, determine the behavioral performance of soft robots in response to external stimuli. Multi-material topology optimization [47–50] provides a promising avenue to

guide our design of soft robots in both material and geometry aspects. Zhang et al. [51,52] integrated soft actuating material and hard elastic material into one soft finger to achieve maximal bending deflection without sacrificing the load-carrying capability. Hiller and Lipson [53] optimized the distribution of hard and soft materials in a cantilever beam so as to program the predefined profiles. Sundaram et al. [54] implemented topology optimization to design the actuator composed of soft and rigid polymers and the designed magnetic polymer composite could react with a magnetic field. Moreover, a 4D printed gripper consisting of active and passive materials was designed to match the given target displacement with the help of the density-based topology optimization method [38]. Recently, Tian et al. [55,56] employed the conformal topology optimization on ferromagnetic soft active structures using the extended level set method (XLSM), and this optimization method was verified on a flytrap gripper with a single material. Inspired by the variable stiffness laminate (VSL) [57–59], where the fiber orientation is spatially varied, the multi-material ferromagnetic soft active structures with multiple magnetic directions is designed in this study. In addition, the design of this type of ferromagnetic soft active structure with multiple magnetization orientations also takes manufacturing into consideration . Stereolithography will be adopted to fabricate the optimized designs owing to its unique characteristics. During the printing process, the light projector can emit the UV light on the selected region of the substrate, and this region could be the one constituent phase with a specific magnetization direction.

While soft materials are capable of large deformations with material and geometric nonlinearities under a given load, numerical instabilities and convergence issues inevitably occur in the nonlinear optimization process [60]. A common practice for optimizing the structural topology optimization of hyperelasticity is a two-step process where linear optimization is first performed to obtain an approximate solution. This linear solution is then used as an initial design for the subsequent nonlinear optimization [61,62]. To avoid convergence difficulties and to reduce the computational cost, we assume that the material is linear elastic in this paper.

In this study, the newly proposed extended level set method (X-LSM) [24] and conformal geometry theory [63–66] are employed to carry out topology optimization of ferromagnetic soft active structures that are modeled mathematically as manifolds. The reconciled level set method [67–69] is used to design a multi-material ferromagnetic active structure. It should be noted that the designed structure is stimulated by a magnetic field, which results in a magnetic body force with details provided in Section 2. This optimization problem becomes a design-dependent problem as the magnetic load changes over time as the design evolves through the optimization process [60,70,71].

To validate the performance of the optimized results, STereo-Lithography (STL) files for the conformal topology optimization results are built subsequently. Researchers, for example, Zegard and Paulino [72] and Liu and Tovar [73] have done the STL file generation of 2D planar topology optimization results. Vogiatzis and Chen et al. [74] developed a level-set-based framework that can generate the STL files and offer post-processing work. Creating STL files for conformal topology optimization results in the form of manifolds is a more challenging task. Vogiatzis et al. [75] proposed a computational framework that can design metasurface by combining level-set-based topology optimization with conformal geometry theory. In this study, the conformal geometry theory will also be utilized to generate the STL files for optimized conformal ferromagnetic soft active structures.

The remainder of this paper is organized as follows: Section 2 introduces the ferromagnetic soft material (FSM) based actuation mechanism. Section 3 presents details on the topology optimization for conformal ferromagnetic soft active structures, including the conventional level set method, X-LSM with conformal geometry theory, reconciled level set method, problem formulation, and shape sensitivity analysis. Section 4 provides several numerical examples, followed by numerical verification and functional 3D printing presented in Section 5 and Section 6, respectively. Section 7 concludes the paper and outlines future work.

2. Actuation mechanism and FEA modeling

2.1. Actuation mechanism of ferromagnetic soft material

In this section, we summarize the actuation mechanism of the ferromagnetic soft material (FSM) and present the governing equations of magnetism, in so far as necessary for the development of this paper. For details, the readers are referred to [76] and the references therein.

First, consider an external magnetic field $\boldsymbol{H}$ generated by a electromagnetic coil in air, as shown in Fig. 2. According to the Biot–Savart in Eq. (1), the resultant magnetic flux density $\boldsymbol{B}^*$ at position $\boldsymbol{p}$ in 3D-space generated

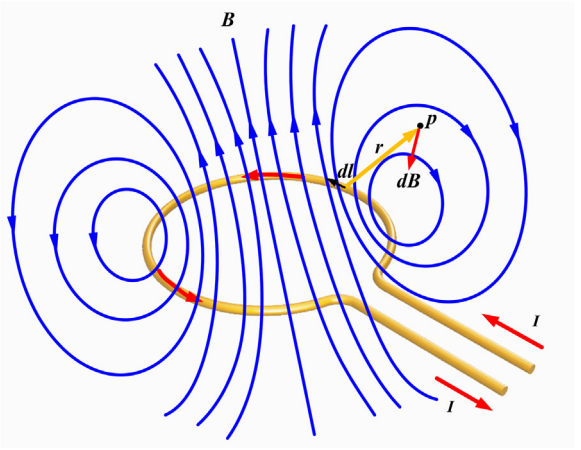

Fig. 2. A wire coil carrying a current $\boldsymbol{I}$ produces a magnetic field at point p given by the Biot–Savart law.

by a current I due to the electromagnetic coils can be calculated as

$$\boldsymbol{B}^*(\boldsymbol{x}) = \frac{\mu_0}{4\pi}\int_C \frac{I\, d\boldsymbol{l}\times\boldsymbol{r}}{|\,\boldsymbol{r}\,|^3}, \tag{1}$$

where $d\boldsymbol{l}$ is the differential element vector along the coil path C, pointing to the current direction. $\boldsymbol{r}$ is the displacement from the differential element to the position $\boldsymbol{p}$. μ_0 denotes the air permeability. In the current-free space, the Maxwell's equations governing a static magnetic field are given by

$$\boldsymbol{B}^* = \mu_0 \boldsymbol{H}, \tag{2a}$$

$$curl(\boldsymbol{H}) = \boldsymbol{0}. \tag{2b}$$

Next, we introduce a ferromagnetic soft polymer with remnant magnetization $\boldsymbol{M}$ to be placed in a certain region of the current-free space, as shown in Fig. 3. Based on the physical observation [77], the magnetic flux density $\boldsymbol{B}$ of the ferromagnetic soft material is linearly related to the applied magnetic field $\boldsymbol{H}$ when the field strength is far below the coercivity of the embedded ferromagnetic particles [19], which can be expressed as

$$\boldsymbol{B} = \mu_0\,(\boldsymbol{H} + \boldsymbol{M})\,. \tag{3}$$

Hence, the Maxwell equations governing the magnetic field within this magnetic polymer are formulated as

$$\nabla\cdot\boldsymbol{B} = 0, \tag{4a}$$

$$curl\left(\frac{1}{\mu_0}\boldsymbol{B} - \boldsymbol{M}\right) = \boldsymbol{0}. \tag{4b}$$

Then, the magnetic potential energy per unit volume of the ferromagnetic soft material can be defined as

$$W = -\boldsymbol{M}\cdot\boldsymbol{B}^*. \tag{5}$$

Finally, the magnetic torque $\boldsymbol{\tau}$ is derived from the magnetic potential energy as follows:

$$\boldsymbol{\tau} = -\frac{dW}{d\theta} = \boldsymbol{M}\times\boldsymbol{B}^*, \tag{6}$$

where θ is the angle between the vectors of magnetization and applied magnetic flux density. It should be noted that this magnetic field must be uniform because the magnetic torques are generated only in a uniform magnetic field.

For the sake of generality, a non-uniform magnetic field is considered here. The torque caused by a uniform magnetic field is equivalently replaced with a magnetic body force to stimulate the ferromagnetic soft material. The magnetic body force $\boldsymbol{F}_m$ is calculated as [13,21]

$$\boldsymbol{F}_m = \mu_0\,(\boldsymbol{M}\cdot\nabla)\,\boldsymbol{H}. \tag{7}$$

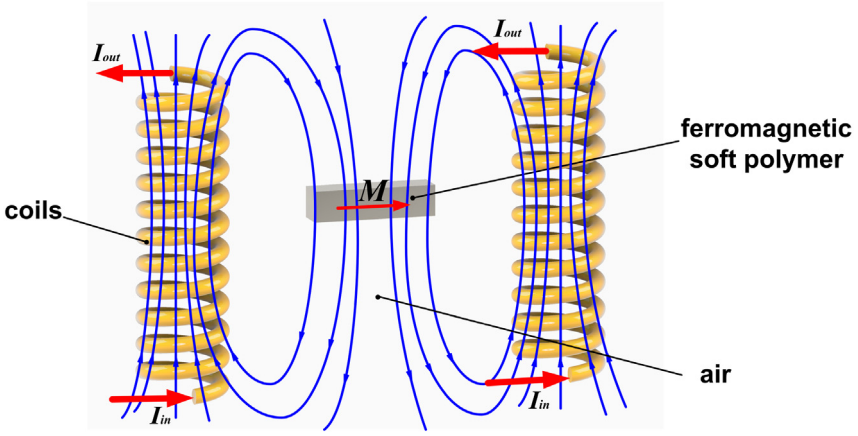

Fig. 3. Schematic representation of a ferromagnetic soft material placed in a magnetic field.

Rewriting the magnetic force with index notation results in the following scalar-valued function of the magnetic force:

$$F_{mi} = \mu_0 \left(M_x \frac{\partial H_i}{\partial x} + M_y \frac{\partial H_i}{\partial y} + M_z \frac{\partial H_i}{\partial z} \right), \tag{8}$$

where H_i is the component of magnetic field intensity in the ith direction; M_x, M_y and M_z are the components of magnetization in x, y, and z direction respectively.

From Eqs. (3) and (7), it is noted that the magnetic field and the mechanics field are coupled bilaterally. Specifically, the emergence of the ferromagnetic soft material will disturb the external magnetic field, which in turn affects the force applied to the ferromagnetic soft material. To simplify the problem, we assume that the ferromagnetic soft structure does not significantly alter the external magnetic field. Correspondingly, a mutual-coupling model is transformed into a one-way coupling model.

2.2. Definition of magnetization direction

In this study, the soft polymer in which the ferromagnetic particles are dispersed exists as a free-form surface or manifolds. Before the ferromagnetic soft polymer is exposed to a strong magnetic field, the ferromagnetic particles are randomly dispersed in the soft polymer, and there is no magnetization. Therefore, a certain direction of the external magnetic field needs to be selected to tune the net magnetic moment of the soft polymer surface.

Now consider a surface $S \subset \mathbb{R}^3$ that can be parameterized by two variables s_1 and s_2 as follows:

$$\boldsymbol{S}(s_1, s_2) = x(s_1, s_2)\boldsymbol{i} + y(s_1, s_2)\boldsymbol{j} + z(s_1, s_2)\boldsymbol{k}, \tag{9}$$

where x, y, z are based on the global Cartesian coordinate system. The relationship between x, y, z and s_1, s_2 is usually nonlinear. The unit tangent vectors $\boldsymbol{t}_1$ and $\boldsymbol{t}_2$ that define a tangent plane at any point $P(x, y, z)$ on the surface S are given as follows:

$$\boldsymbol{t}_1 = k_1 \left(\frac{\partial x(s_1, s_2)}{\partial s_1}\boldsymbol{i} + \frac{\partial y(s_1, s_2)}{\partial s_1}\boldsymbol{j} + \frac{\partial z(s_1, s_2)}{\partial s_1}\boldsymbol{k} \right), \tag{10a}$$

$$\boldsymbol{t}_2 = k_2 \left(\frac{\partial x(s_1, s_2)}{\partial s_2}\boldsymbol{i} + \frac{\partial y(s_1, s_2)}{\partial s_2}\boldsymbol{j} + \frac{\partial z(s_1, s_2)}{\partial s_2}\boldsymbol{k} \right), \tag{10b}$$

where k_i is the normalizing parameters. It follows that the surface unit normal is given by

$$\boldsymbol{n} = \frac{\boldsymbol{t}_1 \times \boldsymbol{t}_2}{\|\boldsymbol{t}_1 \times \boldsymbol{t}_2\|}. \tag{11}$$

Let us take the Torus surface as an example. A Torus can be parametrically defined by $\boldsymbol{S}(u, v) = (R + r\cos u)\cos v\, \boldsymbol{i} + (R + r\cos u)\sin v\, \boldsymbol{j} + r\sin u\, \boldsymbol{k}$. The two tangent variables and the normal to the Torus surface can be calculated according to Eqs. (10), (11) and the directions are shown in Fig. 4.

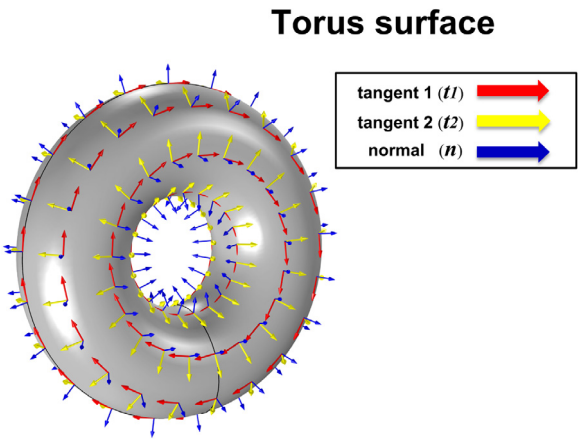

Fig. 4. A schematic of tangent and normal directions on a Torus surface.

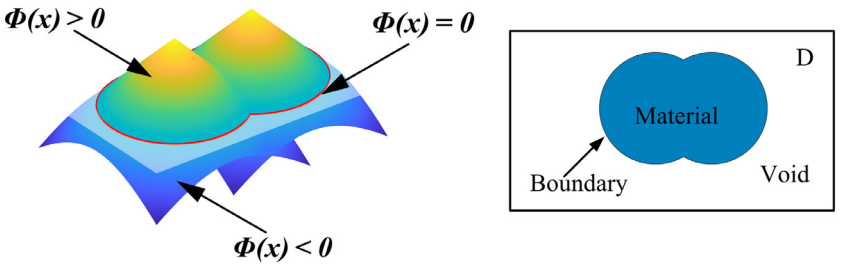

Fig. 5. A schematic of the level set representation.

In this paper, the net magnetic moment of the soft polymer on surface are all defined along the tangent directions $\boldsymbol{t}_1$, $\boldsymbol{t}_2$ or normal direction $\boldsymbol{n}$.

3. Topology optimization of conformal ferromagnetic soft active structures

3.1. Conventional level-set-based topology optimization

Conventionally, the level set function Φ is a Lipschitz continuous real-valued function defined in $\mathbb{R}^2$ or $\mathbb{R}^3$ [61]. The boundary of the design $\partial\Omega$ is implicitly represented as the zero level set of the function Φ, as illustrated in Fig. 5. According to the sign of the level set function, the design domain can be divided into three parts: the material, the interface, and the void. The properties of the level set function can be formulated as Eq. (12):

$$\begin{cases} \Phi(x,t) > 0, & x \in \Omega, \quad \text{material} \\ \Phi(x,t) = 0, & x \in \partial\Omega, \quad \text{boundary} \\ \Phi(x,t) < 0, & x \in D \backslash \Omega, \quad \text{void} \end{cases} \tag{12}$$

where D represents the design domain. The dynamics of the boundary evolution is described by the Hamilton–Jacobi equation:

$$\frac{\partial \Phi(x,t)}{\partial t} - V_n |\nabla \Phi(x,t)| = 0, \tag{13}$$

where V_n is the normal velocity field.

3.2. Reconciled level set method for multi-material topology optimization

In this section, the reconciled level set (RLS) method for designing the multi-material ferromagnetic soft active structures is introduced. Due to the difficulties of fabrication, a ferromagnetic soft active structure with

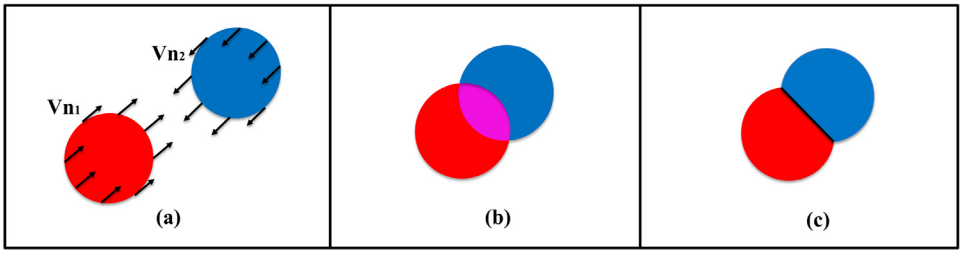

Fig. 6. Schematic of the reconciled level set method. (a) Two materials moving in opposite directions at the same speed; (b) Overlapped materials; (c) Reconciled level set with MBO operator applied. (For interpretation of the references to color in this figure legend, the reader is referred to the web version of this article.)

continuously varying magnetization direction is not considered in this study [78]. Alternatively, in order to assure the manufacturability, a multi-material ferromagnetic soft active structure consisting of several segmented magnetized phases with different uniform magnetization directions is preferred to design [79]. Thus, the multi-material topology optimization becomes a reasonable option to implement the design of this kind of multi-material ferromagnetic soft active structures.

The 'Color' level set (CLS) method [41,50] and the reconciled level set (RLS) method [67–69] are the two main approaches being widely used to design multi-material structure within the level set framework. The 'Color' level set (CLS) method uses the combined signs of n level set function to represent up to 2^n materials, whereas the reconciled level set (RLS) method uses n level set functions to represent n material phase. Compared with the CLS method, the RLS method provides a more straightforward way to implement the multi-material topology optimization, since each material phase is uniquely represented by an independent level set function. For the CLS method, the combined level set function for each material is no longer a signed distance function. This makes the CLS method not that direct and convenient for specifying the design velocities on each level set function [80]. Thus, the reconciled level set (RSL) method is employed for multi-material topology optimization of ferromagnetic soft active structures in this study. During the boundary evolution process, changes in each level set function may result in overlaps between different material phases. This problem can be resolved by applying the Merriman–Bence–Osher (MBO) operator [81,82] to the level set function for each material phase i:

$$\widetilde{\Phi}_i = 0.5\left(\Phi_i^* - \max_{i\neq j}\Phi_j^*\right), \tag{14}$$

where Φ_i^* represents the level set after evolution and $\widetilde{\Phi}_i$ is the level set function after applying MBO operator. The subscripts i and j denote the different materials.

Fig. 6 is plotted to clearly illustrate the boundary evolution process of two level set functions representing two constituent materials. Initially, the red and blue circles are located at a certain distance away. Represented by two independent level set functions, the red and blue circles are moving towards one the other at their own speed V_{n1} and V_{n2} before intersecting and overlapping together. With the MBO operator applied, a clear boundary emerges between the two coupled level set functions.

With the reconciled level set method, the interpolated properties $\boldsymbol{D}^*$ with k constituent materials can be expressed as

$$\boldsymbol{D}^* = \sum_{j=1}^{k} H(\Phi_j)\boldsymbol{D}_j + \prod_{j=1}^{k}\left(1 - H(\Phi_j)\right)\boldsymbol{D}_0, \tag{15}$$

where $\boldsymbol{D}_j$ represents the material properties of jth constituent and $H(\Phi_j)$ is the Heaviside function of the level set function Φ_j. $\boldsymbol{D}_0$ denotes the dummy material properties. The symbol $\boldsymbol{D}$ represents the material properties and it can be Young's modulus, magnetization or density. According to Eq. (8), the interpolated magnetic body force F_{mi}^*

with k constituent ferromagnetic materials can be calculated as

$$\begin{aligned} F_{mi}^{*} = \mu_0 & \left(\sum_{j=1}^{k} H(\Phi_j) \boldsymbol{M}_j \cdot \boldsymbol{e}_x + \prod_{j=1}^{k} \left(1 - H(\Phi_j)\right) \boldsymbol{M}_0 \cdot \boldsymbol{e}_x \right) \frac{\partial H_i}{\partial x} \\ + \mu_0 & \left(\sum_{j=1}^{k} H(\Phi_j) \boldsymbol{M}_j \cdot \boldsymbol{e}_y + \prod_{j=1}^{k} \left(1 - H(\Phi_j)\right) \boldsymbol{M}_0 \cdot \boldsymbol{e}_y \right) \frac{\partial H_i}{\partial y} \\ + \mu_0 & \left(\sum_{j=1}^{k} H(\Phi_j) \boldsymbol{M}_j \cdot \boldsymbol{e}_z + \prod_{j=1}^{k} \left(1 - H(\Phi_j)\right) \boldsymbol{M}_0 \cdot \boldsymbol{e}_z \right) \frac{\partial H_i}{\partial z}, \end{aligned} \tag{16}$$

where $\boldsymbol{M}_j$ represents the magnetization of *jth* constituent ferromagnetic material and $\boldsymbol{M}_0$ denotes the magnetization of the dummy material. $\boldsymbol{e}_x$, $\boldsymbol{e}_y$ and $\boldsymbol{e}_z$ denote the three unit base vectors in a three-dimensional Cartesian space.

3.3. Conformal topology optimization on manifolds using Extended Level Set Method (X-LSM)

Many bionic soft active structures exist as curved thin-shell structures, or manifolds in a mathematical term. The conventional level set method only works in the Euclidean space where the design domain is flat. How to implement level-set-based conformal topology optimization on a manifold is an important but challenging issue. Ye et al. [24,83] have systematically addressed the issue of structural shape and topology optimization on freeform surface by proposing an extended level set method (X-LSM) using the conformal geometry theory [63,64]. Conventional level-set-based topological optimization can only be carried out in Euclidean domains, by using conformal geometry theory, the level set method can be generalized to the manifold domains.

For completeness, the main theoretical concepts of conformal geometry theory are presented here. The conformal geometry gives the mapping relationship between two Riemannian manifolds [84]. A Riemannian manifold can be defined as a smooth manifold with a Riemannian metric $\mathbf{p}$, which can be defined as

$$\mathbf{p} = e^{2\mu(x,y)} \left(dx^2 + dy^2\right), \tag{17}$$

where (x, y) is the isothermal coordinates.

Suppose given two Riemannian surfaces $(S_1, \mathbf{p}_1)$ and $(S_2, \mathbf{p}_2)$, where $\mathbf{p}_1$ and $\mathbf{p}_2$ are Riemannian metric tensors, a smooth mapping φ: $S_1 \to S_2$ is called as conformal if the pull-back metric induced by φ and the original metric differ by a scalar function. Specifically, there exists a conformal factor μ: $S \to \mathbb{R}$, such that

$$\varphi^{*}\mathbf{p}_2 = e^{2\mu}\mathbf{p}_1. \tag{18}$$

Thus, conformal mapping is essentially a local scaling transformation governed by a scalar function $e^{2\mu}$.

The distinguishing feature of conformal mapping is that it conserves orientation and angles locally. As illustrated in Fig. 7, the orthogonal angles of the checkerboard patterns on the 2D plane is well preserved on a human face freeform surface after mapping. The conformal mapping provides the point-to-point relation between the manifold and the 2D plane in the Euclidean space [84].

By employing the conformal geometry theory, we can conformally parameterize a triangle meshed manifold onto a 2D rectangular domain where the level set function is defined. Owing to the point-to-point relation between the manifold and the 2D plane, the corresponding level set function value on the manifold can be calculated through interpolation before we do the finite element analysis of ferromagnetic soft active structures. After solving the equilibrium on the manifold, the shape sensitivity is calculated, and the design velocity field is constructed subsequently. Finally, we can evolve the design on the plane using the modified Hamilton–Jacobi equation as follows [24]:

$$\frac{\partial \Phi(x,t)}{\partial t} - e^{-\mu} V_n |\nabla \Phi(x,t)| = 0, \tag{19}$$

where the μ is the *conformal factor* quantifying the scaling effect of the conformal mapping. In this way, the X-LSM can transform a conformal topology optimization problem on Riemannian manifolds in 3D space to a 2D topology optimization problem in Euclidean space. It is worth noting that only with the conformal mapping can we attain such a concise Euclidean representation of the level set equation on the manifold, which otherwise would be too complicated and computationally formidable.

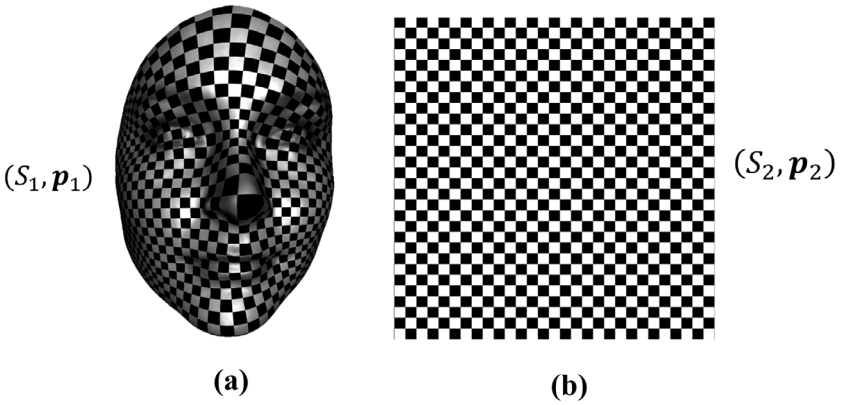

Fig. 7. Conformal geometry from the 3D surface to the 2D plane preserves the Checkerboard patterns. (a) The Checkerboard patterns on a 3D surface. (b) The Checkerboard patterns on a 2D plane.

The X-LSM using conformal geometry theory is the first to be proposed and employed into the design of soft active shell structures in this study. Our proposed method can guarantee the optimization problem on the manifolds and the 2D plane are mathematically equivalent. By reducing the dimension from 3D manifolds to 2D Euclidean space, the computational costs save dramatically. In addition, this proposed method can be effortlessly coupled with the conventional level set framework. The reconciled level set (RLS) method can be combined with the proposed method to solve multi-material topology optimization problem on manifolds. In this way, the advantage of the conventional level set method including generating clear and smooth boundaries can be retained.

3.4. Problem formulation

Through shape morphing, the ferromagnetic soft active structure aims to deliver the desirable kinematic behaviors. Meanwhile, the soft active structure itself should have sufficient stiffness to sustain the interaction force when interacting with objects. Here, the commonly used criterion for the design of the compliant mechanisms, the least square errors compared with the target displacement [61,85,86], is chosen as a sub-objective function for the kinematic requirement. For linear elastic materials, the stiffness can be represented by one of these three quantities, including strain energy, end compliance, or the complementary work [62]. Among them, the end compliance is selected to characterize stiffness in this paper. Therefore, the design problem for a conformal ferromagnetic soft active structure can be formulated as a balance of desired kinematic requirement and structural stiffness, shown as follows:

$$\begin{aligned} Minimize: \quad J =& w_1 \left(\int_{\Omega} \boldsymbol{g} \cdot \boldsymbol{u} \mathrm{d}\Omega + \int_{\Gamma_N} \boldsymbol{f} \cdot \boldsymbol{u} \mathrm{d}s \right) \\ &+ w_2 \left(\int_{\Omega} k| \boldsymbol{u} - \boldsymbol{u}_0|^2 \mathrm{d}\Omega \right)^{\frac{1}{2}}, \\ Subject\ to: \quad & a(\boldsymbol{u}, \boldsymbol{v}) = l(\boldsymbol{v}), \quad \forall \boldsymbol{v} \in U \\ & V(\Omega) = V^*, \end{aligned} \tag{20}$$

where U stands for the space of kinematically admissible displacement fields [87]; $\boldsymbol{u}_0$ denotes the target displacement field; $\boldsymbol{u}$ denotes the actual displacement field; Ω indicates the material region in the design domain D. The boundary of the design is denoted by Γ, which comprises segments with Neumann boundary condition Γ_N, Dirichlet boundary condition Γ_D, and free boundary $\partial\Omega$. $\boldsymbol{g}$ and $\boldsymbol{f}$ denote the body force (red arrows) acting on the soft body and the traction force (blue arrows) acting on the Neumann boundary Γ_N respectively, as illustrated in Fig. 8. $V(\Omega)$ is the volume of the soft body, and V^* is the target volume. Localizing factor k is used to select the area of concern for kinematic performance, where it is equal to 1. Except in this area, the localizing factor k is zero. w_1 and w_2 are weighting factors for end compliance and kinematic target, respectively. Excessive kinematic weighting factor ω_2 tends to cause the structure discontinuity during the optimization process, which makes the structure has no loading capability. Thus, the selection of weighting factors follows the principle that the end compliance and the least square

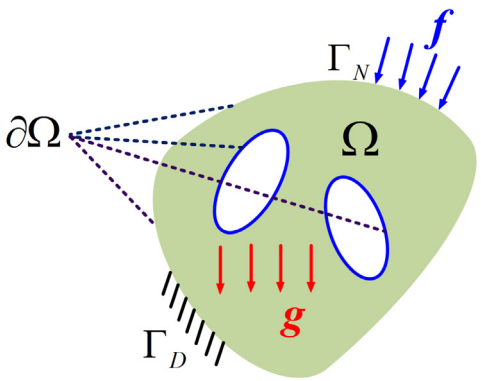

Fig. 8. A schematic of general boundary condition. (For interpretation of the references to color in this figure legend, the reader is referred to the web version of this article.)

error compared to the target displacement have a relatively closer order of magnitude. Here, $a(\boldsymbol{u}, \boldsymbol{v}) = l(\boldsymbol{v})$ is the weak form of governing equation. The energy form $a(\boldsymbol{u}, \boldsymbol{v})$ and the load form $l(\boldsymbol{v})$ as well as the volume $V(\Omega)$ are defined as

$$a(\boldsymbol{u}, \boldsymbol{v}) = \int_{\Omega} \epsilon_{ij}^{T}(\boldsymbol{u}) \mathbb{C}_{ijkl} \epsilon_{kl}(\boldsymbol{v}) \mathrm{d}\Omega, \tag{21a}$$

$$l(\boldsymbol{v}) = \int_{\Omega} \boldsymbol{g} \cdot \boldsymbol{v} \mathrm{d}\Omega + \int_{\Gamma_N} \boldsymbol{f} \cdot \boldsymbol{v} \mathrm{d}s, \tag{21b}$$

$$V(\Omega) = \int_{D} H(\Phi) \mathrm{d}\Omega, \tag{21c}$$

where ϵ is the second-order linear strain tensor; $\mathbb{C}_{ijkl}$ is a fourth-order elastic stiffness tensor; $H(\Phi)$ represents the Heaviside function.

3.5. Shape sensitivity analysis

Topology optimization of conformal ferromagnetic soft active structures is a typical PDE-constrained optimization problem. The method of Lagrange multipliers is employed to reformulate the PDE-constrained problem into an unconstrained optimization problem by coupling the objective function and governing equation as follows:

$$L(\boldsymbol{u}, \boldsymbol{v}) = J + \lambda \left(a(\boldsymbol{u}, \boldsymbol{v}) - l(\boldsymbol{v}) \right), \tag{22}$$

where the λ is a Lagrange multiplier, and $\boldsymbol{v}$ is the adjoint displacement. Material time derivative is used to derive the shape sensitivity [61,87,88]:

$$\frac{DL(\boldsymbol{u}, \boldsymbol{v})}{Dt} = \frac{DJ}{Dt} + \frac{Da(\boldsymbol{u}, \boldsymbol{v})}{Dt} - \frac{Dl(\boldsymbol{v})}{Dt}. \tag{23}$$

The material time derivative of the objective function J is given by

$$\begin{aligned}
\frac{DJ}{Dt} &= \frac{\partial J}{\partial t} + \frac{\partial J}{\partial \Omega} \\
&= \omega_1 \left(\int_{\Omega} \boldsymbol{g} \cdot \boldsymbol{u}' \mathrm{d}\Omega + \int_{\Gamma_N} \boldsymbol{f} \cdot \boldsymbol{u}' \mathrm{d}s \right) \\
&+ \omega_2 \left(\int_{\Omega} k |\, \boldsymbol{u} - \boldsymbol{u}_0|^2 \mathrm{d}\Omega \right)^{\frac{-1}{2}} \int_{\Omega} k (\boldsymbol{u} - \boldsymbol{u}_0)^T \boldsymbol{u}' \mathrm{d}\Omega \\
&+ \omega_1 \int_{\Gamma} \boldsymbol{g} \cdot \boldsymbol{u} \boldsymbol{V}_n \mathrm{d}s + \omega_1 \int_{\Gamma} \left(\frac{\partial (\boldsymbol{f} \cdot \boldsymbol{u})}{\partial \boldsymbol{n}} + \kappa (\boldsymbol{f} \cdot \boldsymbol{u}) \right) \boldsymbol{V}_n \mathrm{d}s \\
&+ \frac{1}{2} \omega_2 \left(\int_{\Omega} k |\, \boldsymbol{u} - \boldsymbol{u}_0|^2 \mathrm{d}\Omega \right)^{\frac{-1}{2}} \int_{\Gamma} k |\, \boldsymbol{u} - \boldsymbol{u}_0|^2 \boldsymbol{V}_n \mathrm{d}s.
\end{aligned} \tag{24}$$

The material time derivative of the energy form $a(\boldsymbol{u}, \boldsymbol{v})$ and the load form $l(\boldsymbol{u}, \boldsymbol{v})$ can be expressed as Eqs. (25) and (26) respectively,

$$\begin{aligned}\frac{Da}{Dt} =&\frac{\partial a}{\partial t} + \frac{\partial a}{\partial \Omega}\\ =&\int_{\Omega} \epsilon_{ij}^{T}(\boldsymbol{u}')\mathbb{C}_{ijkl}\epsilon_{kl}(\boldsymbol{v})\mathrm{d}\Omega + \int_{\Omega} \epsilon_{ij}(\boldsymbol{u})\mathbb{C}_{ijkl}\epsilon_{kl}(\boldsymbol{v}')\mathrm{d}\Omega\\ &+ \int_{\Gamma} \epsilon_{ij}(\boldsymbol{u})\mathbb{C}_{ijkl}\epsilon_{kl}(\boldsymbol{v})\boldsymbol{V}_n\mathrm{d}s.\end{aligned} \tag{25}$$

$$\begin{aligned}\frac{Dl}{Dt} =&\frac{\partial l}{\partial t} + \frac{\partial l}{\partial \Omega}\\ =&\int_{\Omega} \boldsymbol{g}\cdot\boldsymbol{v}'\mathrm{d}\Omega + \int_{\Gamma_N} \boldsymbol{f}\cdot\boldsymbol{v}'\mathrm{d}s + \int_{\Gamma} \boldsymbol{g}\cdot\boldsymbol{v}\boldsymbol{V}_n\mathrm{d}s\\ &+ \int_{\Gamma}\left(\frac{\partial\left(\boldsymbol{f}\cdot\boldsymbol{v}\right)}{\partial \boldsymbol{n}} + \kappa\left(\boldsymbol{f}\cdot\boldsymbol{v}\right)\right)\boldsymbol{V}_n\mathrm{d}s.\end{aligned} \tag{26}$$

The adjoint equation is constructed by collecting all the terms containing $\boldsymbol{u}'$ from Eqs. (24) to (26), which yields,

$$\begin{aligned}&\int_{\Omega} \epsilon_{ij}^{T}(\boldsymbol{u}')\mathbb{C}_{ijkl}\epsilon_{kl}(\boldsymbol{v})\mathrm{d}\Omega + \omega_1\left(\int_{\Omega}\boldsymbol{g}\cdot\boldsymbol{u}'\mathrm{d}\Omega + \int_{\Gamma_N}\boldsymbol{f}\cdot\boldsymbol{u}'\mathrm{d}s\right)\\ &+ \omega_2\left(\int_{\Omega} k|\ \boldsymbol{u}-\boldsymbol{u}_0|^2\mathrm{d}\Omega\right)^{\frac{-1}{2}}\int_{\Omega} k(\boldsymbol{u}-\boldsymbol{u}_0)^T\boldsymbol{u}'\mathrm{d}\Omega = 0.\end{aligned} \tag{27}$$

Here, the adjoint Eq. (27) can be rewritten as

$$\begin{aligned}&\int_{\Omega} \epsilon_{ij}^{T}(\boldsymbol{v})\mathbb{C}_{ijkl}\epsilon_{kl}(\boldsymbol{u}')\mathrm{d}\Omega\\ =&-\int_{\Omega}\left(\omega_2 D_0 k(\boldsymbol{u}-\boldsymbol{u}_0) + \omega_1\boldsymbol{g}\right)\cdot\boldsymbol{u}'\mathrm{d}\Omega - \omega_1\int_{\Gamma_N}\boldsymbol{f}\cdot\boldsymbol{u}'\mathrm{d}s,\end{aligned} \tag{28}$$

where D_0 is a constant given by

$$D_0 = \left(\int_{\Omega} k|\ \boldsymbol{u}-\boldsymbol{u}_0|^2\mathrm{d}\Omega\right)^{\frac{-1}{2}}. \tag{29}$$

It is worth noticing that the form of Eq. (28) is similar to the weak form of governing equation $a(\boldsymbol{u}, \boldsymbol{v}) = l(\boldsymbol{v})$. Thus, the solution of adjoint variable $\boldsymbol{v}$ can be defined as

$$\begin{cases} -\nabla\cdot\boldsymbol{\sigma}(\boldsymbol{v}) = -D_0 k\left(\boldsymbol{u}-\boldsymbol{u}_0\right) - \boldsymbol{g} & in\ \Omega\\ \boldsymbol{v} = 0 & on\ \Gamma_D\\ \boldsymbol{\sigma}(\boldsymbol{v})\cdot\boldsymbol{n} = \boldsymbol{f} & on\ \Gamma_N\end{cases} \tag{30}$$

where $\boldsymbol{\sigma}$ is the stress tensor.

In our study, since the length of Neumann boundary is zero (the force is applied at a point), the convection terms containing traction force $\boldsymbol{f}$ in Eqs. (24) and (26) can be ignored. For convenience, the $\boldsymbol{v}'$ can be set as zero. After eliminating $\boldsymbol{u}'$ and $\boldsymbol{v}'$, we can formulate the derivative of Lagrangian as follows:

$$\begin{aligned}\frac{DL(\boldsymbol{u}, \boldsymbol{v})}{Dt} =&\omega_1\int_{\Gamma}\boldsymbol{g}\cdot\boldsymbol{u}\boldsymbol{V}_n\mathrm{d}s + \frac{1}{2}\omega_2 D_0\int_{\Gamma} k|\ \boldsymbol{u}-\boldsymbol{u}_0|^2\boldsymbol{V}_n\mathrm{d}s\\ &+ \int_{\Gamma}\epsilon_{ij}(\boldsymbol{u})\mathbb{C}_{ijkl}\epsilon_{kl}(\boldsymbol{v})\boldsymbol{V}_n\mathrm{d}s - \int_{\Gamma}\boldsymbol{g}\cdot\boldsymbol{v}\boldsymbol{V}_n\mathrm{d}s.\end{aligned} \tag{31}$$

With the steepest descent method, the normal design velocity with mean curvature κ and volume constraint can be constructed as

$$\begin{aligned}\boldsymbol{V}_n =&\boldsymbol{g}\cdot\boldsymbol{v} - \omega_1\boldsymbol{g}\cdot\boldsymbol{u} - \frac{\omega_2 D_0}{2}k|\ \boldsymbol{u}-\boldsymbol{u}_0|^2 - \epsilon_{ij}(\boldsymbol{u})\mathbb{C}_{ijkl}\epsilon_{kl}(\boldsymbol{v})\\ &+ \lambda\left(V - V^*\right) + \iota\kappa,\end{aligned} \tag{32}$$

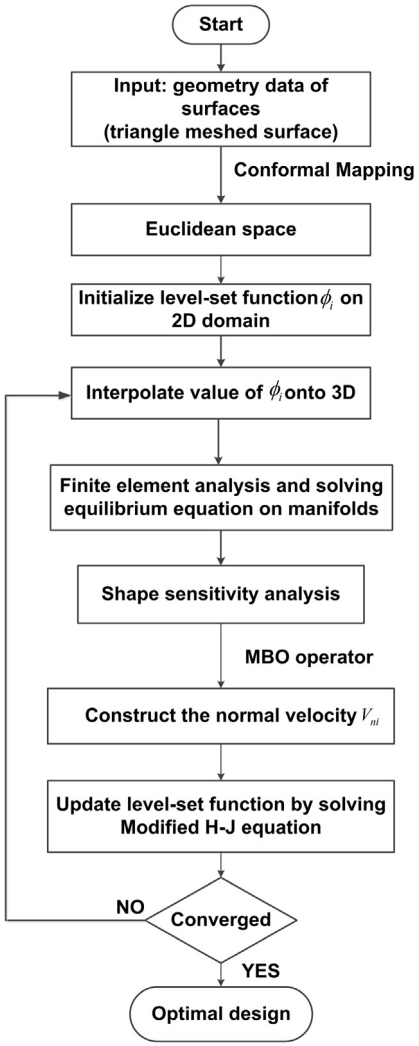

Fig. 9. The flow chart of designing conformal ferromagnetic soft active structures.

where λ and ι are the Lagrange multipliers for volume and perimeter constraint; κ is the curvature of the boundary.

To sum up, the topology optimization process of a conformal ferromagnetic soft active structure can be concluded with a flow chart in Fig. 9.

4. Numerical examples

4.1. Topology optimization of a magnetically-driven gripper with two constituent materials

The first example is to find the optimum design of a ferromagnetic 2-jaw soft gripper structure. Due to the symmetry, only one jaw is studied. As shown in Fig. 10, each jaw is modeled as a cantilever beam (2 m $\times$ 1 m), with its left side clamped. The interaction between the jaw and the object is modeled as a loading $\boldsymbol{p} = (0, 1)$ N and a surface friction $\boldsymbol{f} = (1, 0)$ N, distributed on the contacting area as highlighted by the black area. This black area is also selected as the area of concern for kinematic performance. The localizing factor k is zero except on the black zone where it is equal to 1. The jaw is actuated by a downward external magnetic field with a magnitude of 10 mT. The Young's modulus of both actuating materials keeps the same and is set to $E = 0.1$ MPa. The Poisson's ratio for all materials is set to be 0.3. The magnitudes of the magnetization of both actuating materials are identical with

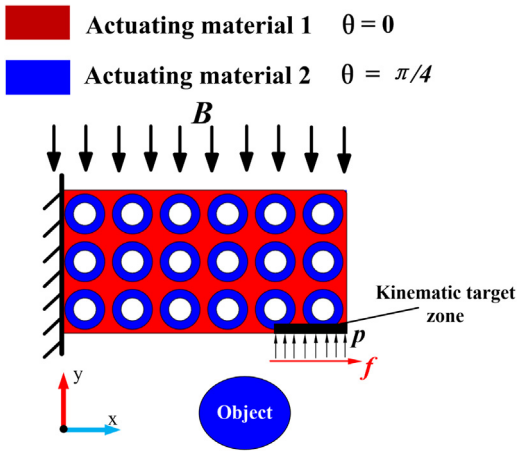

Fig. 10. Boundary conditions of the multi-material ferromagnetic gripper structure.

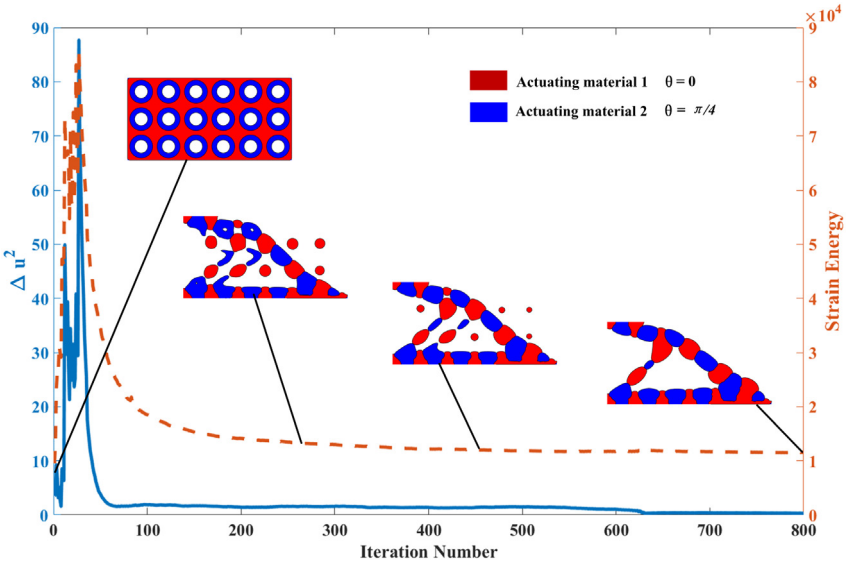

Fig. 11. The optimization history curves and design evolution of the multi-material magnetically-driven gripper.

2.5×10^6 A/m. The only difference between the two actuating materials is the direction of the magnetization, in which one is set to 0° and the other to 45°. Therefore, the angles between magnetic flux density $\boldsymbol{B}$ and magnetization $\boldsymbol{M}$ are 90° and 135°, respectively. The purpose of setting one more actuating material with a larger angle between $\boldsymbol{B}$ and $\boldsymbol{M}$ is for the larger bending deformation. As a consequence, the magnetic body force distributions onto the two constituent materials are completely different. To avoid singularity, a dummy material with Young's modulus $E = 10$ Pa and magnetization $M = 250$ A/m are set for the void. The target displacement u_{y0} is set to be -0.25 m. The weighting factors for the end compliance and the kinematic target are set as $w_1 = 0.02$ and $w_2 = 0.98$.

The whole design domain is discretized with 100×50 grids. The volume fractions of the two constituent materials are both constrained at 20%. The converge curve for the optimization process and the design evolution history are shown in Fig. 11. At the end of the topology optimization, the volumes of actuating material 1 and 2 are 19.92% and 20.05%. The least-square error with respect to the target displacement converges to 0.0580. The magnetization orientations in the optimized design and the deformed configuration under the external magnetic field is shown in Fig. 12. We also extrude the 2D design into a 2.5D design to simulate the grasping process. As shown in Fig. 13, two grippers with opposite magnetization directions are mounted symmetrically on a platform. With the

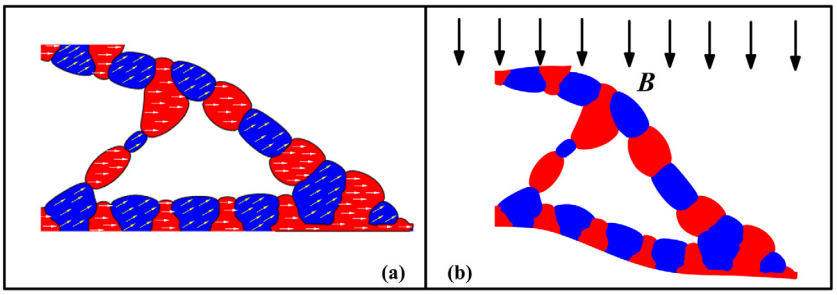

Fig. 12. The magnetization orientations in one jaw of the optimized gripper and its deformed configuration under the external magnetic field. (a) The magnetization orientations in the multi-material ferromagnetic gripper. (b) The bending configuration of the optimized multi-material ferromagnetic gripper under a downward magnetic field.

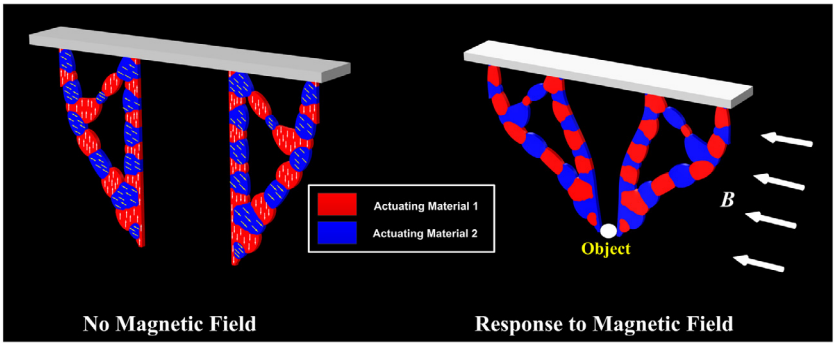

Fig. 13. Simulation of the grasping process of the two-material ferromagnetic gripper.

actuation of the external magnetic field parallel to the platform, the two jaws bend towards the center to grasp the white object. For comparison, the identical boundary condition was applied to the optimized gripper with single magnetization orientation [55]. With the actuation of the applied magnetic field, the displacement u_y in the black area is -0.20 m. Thus, the kinematic performance of the optimized multi-material gripper increased by about 25%.

4.2. Topology optimization of a magnetic soft active structure with three constituent materials

The second example is to solve the optimum design of a magnetic soft active structure with three types of actuating materials. The dimension of design domain is $2\,\text{m} \times 1\,\text{m}$. The details of boundary conditions are shown in Fig. 14, where two endpoints of the bottom edge are fixed. A loading $\boldsymbol{p} = (0, -1)\,\text{N}$ is applied at the contacting area which is highlighted by the black area to model the reaction force given by the object. This black area is also selected as the area of concern for kinematic performance, where the localizing factor k is set as 1. The soft active structure is controlled by an upward external magnetic field with a magnitude of 10 mT. The Young's modulus of all actuating materials keeps the same and is set as $E = 0.1$ MPa. The Poisson's ratio for all materials is set to be 0.3. The magnitudes of the magnetization of three actuating materials are identical with 2.5×10^6 A/m. The magnetization directions of the three actuating materials are set to 0°, 90° and 180°, respectively. In this case, the actuating material with magnetization parallel to the applied magnetic field is for elongation, whereas the actuating material with magnetization perpendicular to the applied magnetic field is for bending. To avoid singularity, a dummy material with Young's modulus $E = 10\,\text{Pa}$ and magnetization $M = 250\,\text{A/m}$ are set for the void. Due to the symmetry, only left half domain is studied. The target displacement u_{y0} is set to be 0.25 m. The weighting factors for the end compliance and the kinematic target are set as $w_1 = 0.05$ and $w_2 = 0.95$.

Due to the symmetry, the design domain is halved to a 1-by-1 square that is discretized with 50×50 grids. The volume fractions of the two constituent materials are both constrained at 20%. The converge curve for the

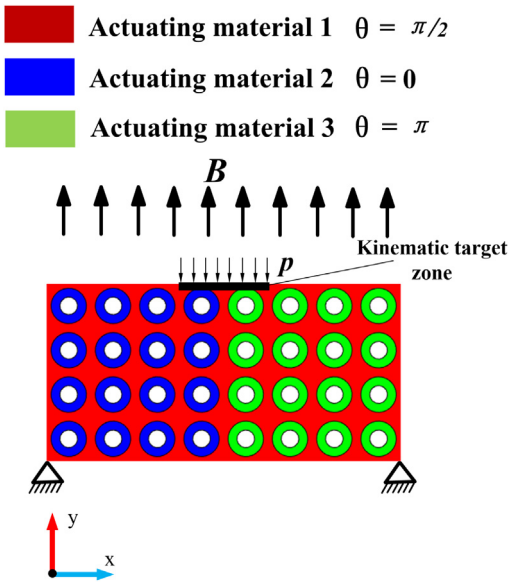

Fig. 14. Boundary conditions of the three-material magnetic soft active structure.

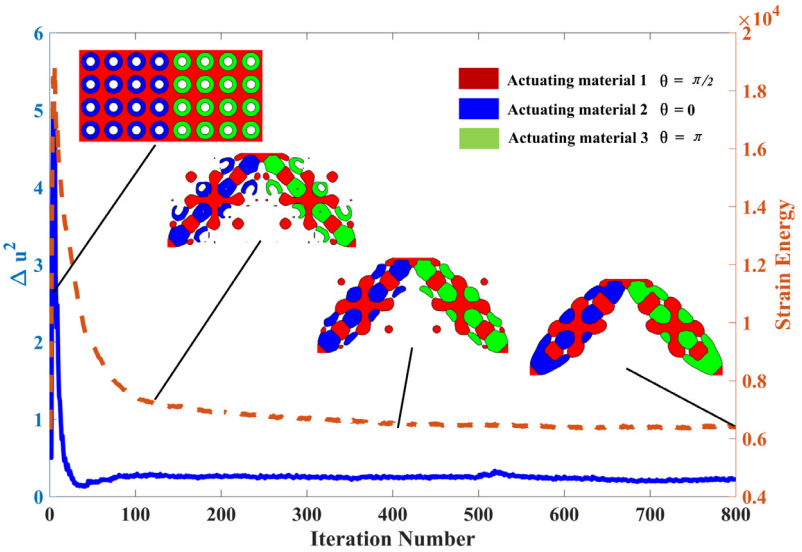

Fig. 15. The optimization history curve and design evolution of the magnetic driven soft active structure.

optimization process and the design evolution history are shown in Fig. 15. The volumes of the actuating material 1 and 2 are 19.95% and 20.11% when the optimization ends. The least-square error with respect to the target displacement converges to 0.1958. The magnetization orientations are plotted on the optimized design and the resultant deformed configuration in response to the external magnetic field is given in Fig. 16. Finally, we extrude the 2D design into a 2.5D design and corresponding deformed configuration is given in Fig. 17.

4.3. Topology optimization of a magnetically driven 6-finger flytrap soft active shell structure

In this section, X-LSM is applied to design a flytrap soft active shell structure, which mimics the flytrap plant in nature. The span of a single petal is approximately 2.5 m × 1.6 m and the thickness is 0.05 m. The target volume

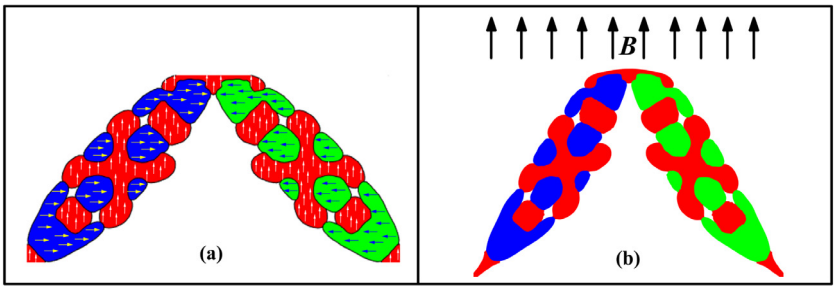

Fig. 16. (a) The magnetization orientations in the three-material ferromagnetic soft active structure. (b) The deformed configuration of the optimized three-material ferromagnetic soft active structure under the external magnetic field.

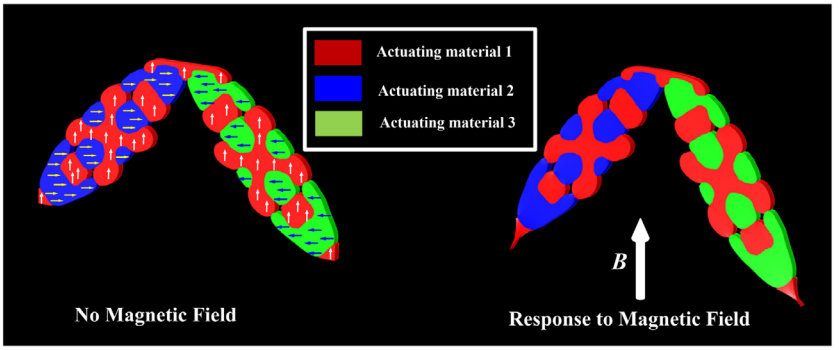

Fig. 17. Simulation of the behavior of three-material soft active structure.

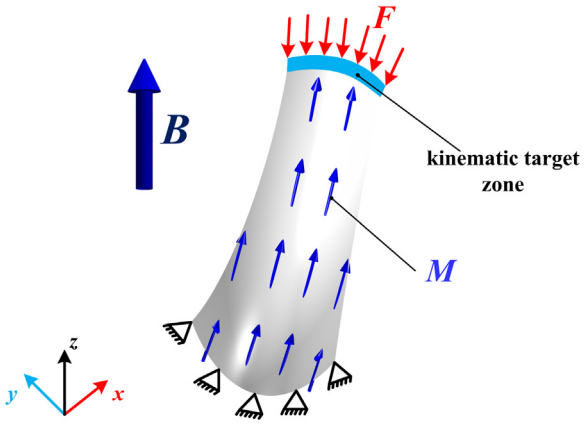

Fig. 18. Boundary condition of flytrap soft active shell structure (only one finger). (For interpretation of the references to color in this figure legend, the reader is referred to the web version of this article.)

ratio is 0.45. The material properties are assumed with a Young's modulus $E = 0.1$ MPa, Poisson's ratio $\mu = 0.3$, and magnetization $M = 8 \times 10^4$ A/m along the shell geometry tangent direction t_1. To avoid singularity, a dummy material with Young's modulus $E = 10$ Pa and magnetization $M = 8$ A/m are set for void. The boundary condition for petal shell is shown in Fig. 18, where the bottom edge is fixed and a interaction force $\boldsymbol{F} = (1, 0, -1)$ N is applied on the top edge. The blue area is chosen as the area of concern for kinematic performance and the target displacement is set as $u_{x0} = -1$ m. The localizing factor k is zero except on the blue area where it is equal to 1. In addition, the weighting factor ω_1 and ω_2 are kept as 0.2 and 0.8, respectively.

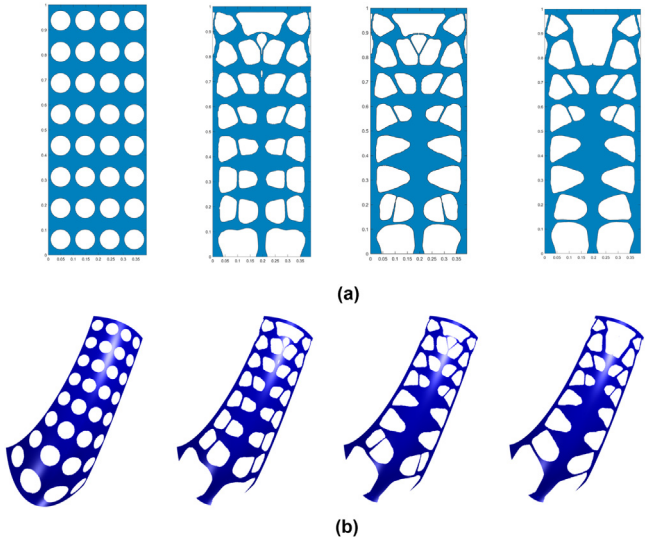

Fig. 19. Design evolution of the flytrap soft active shell structure. (a) Design evolution in 2D. (b) Design evolution on a petal surface.

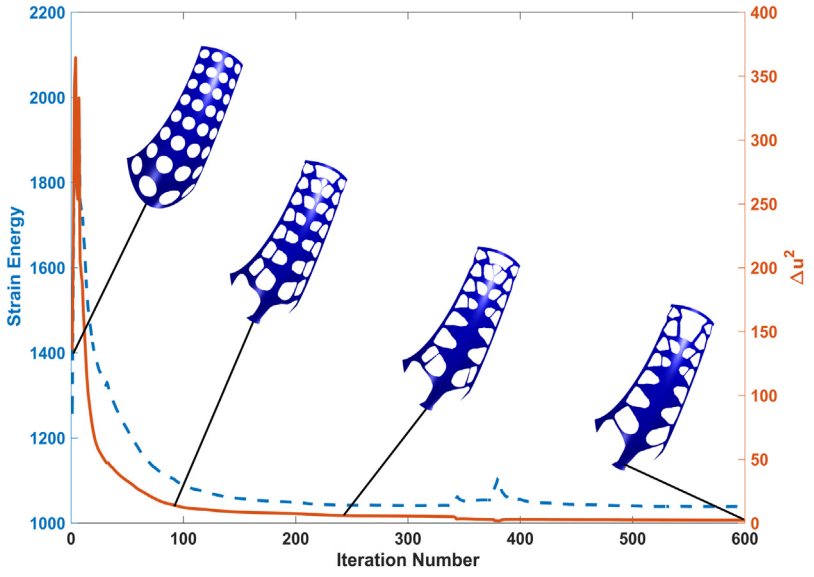

Fig. 20. The optimization history of the flytrap soft active shell structure.

In the optimization process, the petal surface is meshed with 63 422 triangular elements before conformally mapped onto a 0.3923 m $\times$ 1 m 2D rectangular domain where the level set function is defined and discretized with a 197 $\times$ 501 grid. During the implementation, the top layer of the petal is retained by setting design velocity is zero. The 2D design evolution and corresponding evolution on surfaces are shown in Fig. 19. The optimization curves for compliance and target displacement are plotted in Fig. 20. A flytrap structure can be achieved by making a circular pattern of this optimal petal shell structure. The simulation of the behavior of the design is presented in Fig. 21.

In terms of the computational cost, the majority of computational cost is consumed in the 3D finite element analysis (FEA). Each iteration costs approximately 120 s totally and almost 115 s is occupied by 3D finite element analysis. The computational cost of finite element analysis depends on the complexity of geometry model and finite element mesh size. However, the excessively sparse finite element mesh can lead to the inaccuracy of interpolation

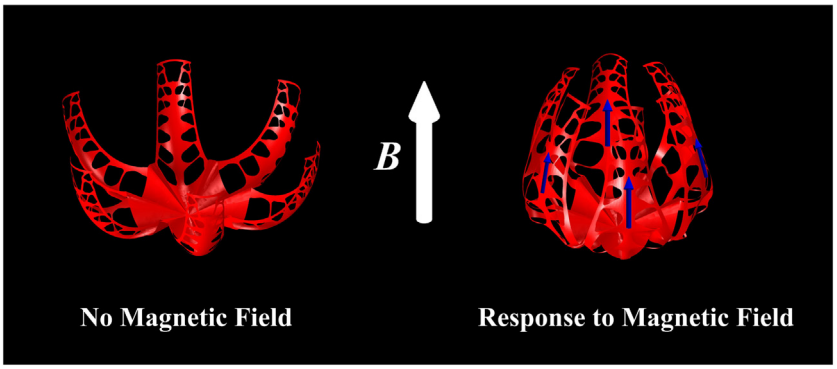

Fig. 21. Simulation of the grasping process of the flytrap soft active shell structure.

between 3D surface and 2D rectangular domain. Thus, the relative dense meshes are used to discretize the surface in this study. In this paper, the proposed X-LSM is building from nothing to solve the structural and shape topology optimization on manifolds. Although the computational cost is brought down by the dimension reduction from 3D to 2D, the dimension reduction work [89] will be continued in the future and get the 3D FEA done in the 2D plane using conformal geometry theory so that the computational cost will reduce further.

4.4. Multi-material topology optimization of a 6-finger magnetically driven flytrap soft active shell structure

In this section, the reconcile level set method is also employed to design the flytrap shell soft active structure with two kinds of materials. One is the elastic material for load carrying, and another material is the ferromagnetic soft material for actuating. The topology optimization design domain and boundary condition keep the same as the single material case, as shown in Fig. 18. The Young's modulus of the elastic material is $E_h = 0.1$ MPa while the actuating material is $E_s = 1000$ Pa. The Poisson's ratio for all materials is set to be 0.3. The magnetization of actuating material is set as $M = 4 \times 10^5$ A/m along the shell geometry tangent direction t_1. To avoid singularity, the magnetization in non-patterned areas is set as $M_0 = 40$ A/m, and the Young's modulus in the void is $E_0 = 1$ Pa. The volume fraction targets for the elastic and actuating material are 0.45 and 0.1, respectively. The target displacement in the concerned area of kinematic performance is still set as $u_{x0} = -1$ m. The weighting factor ω_1 and ω_2 are kept as 0.3 and 0.7, respectively. The initial and final designs in the 2D rectangular domain and the petal surface are shown in Fig. 22, where the blue color refers to the ferromagnetic actuating material and the red color to the elastic material. The grasping process of this multi-material flytrap soft active shell structure is given in Fig. 23.

4.5. Topology optimization of a magnetically driven 6-finger flytrap soft active shell structure with two actuating materials

In the last section, X-LSM combined with the RLS method is also applied to design a flytrap soft active shell structure with multiple actuating materials. As shown in Fig. 24, the magnetization of the two constituent materials are along the shell geometry tangent direction $\boldsymbol{t}_1$ (red arrows) and normal direction $\boldsymbol{n}$ (blue arrows), respectively. The volume fraction targets for both materials are 0.45 and 0.25, respectively. The boundary condition for petal shell is also shown in Fig. 24, where the bottom edge is fixed and an interaction force $\boldsymbol{F} = (1, 0, -1)$ N is applied on the top edge, which keeps the same as the single material case. The blue area is also chosen as the area of concern for kinematic performance, and the target displacement is set as $u_{x0} = -1$ m. The weighting factor w_1 and w_2 are set as 0.2 and 0.8. The material properties for both constituents are assumed with Young's modulus $E = 0.1$ MPa and Poisson's ratio $\mu = 0.3$. The magnitudes of both magnetization are identical with $M = 8 \times 10^4$ A/m. In addition, a dummy material with Young's modulus $E = 10$ Pa and magnetization $M = 8$ A/m are set for the void.

The initial and final designs in the 2D rectangular domain and the petal surface are shown in Fig. 25, where the red and blue areas represent the actuating materials with $\boldsymbol{t}_1$ and $\boldsymbol{n}$ magnetic poles, respectively. Finally, a flytrap soft active shell structure with 6 petals can be constructed by making a circular pattern of the optimized design. Fig. 26 is plotted to illustrate the grasping behavior of the design vividly.

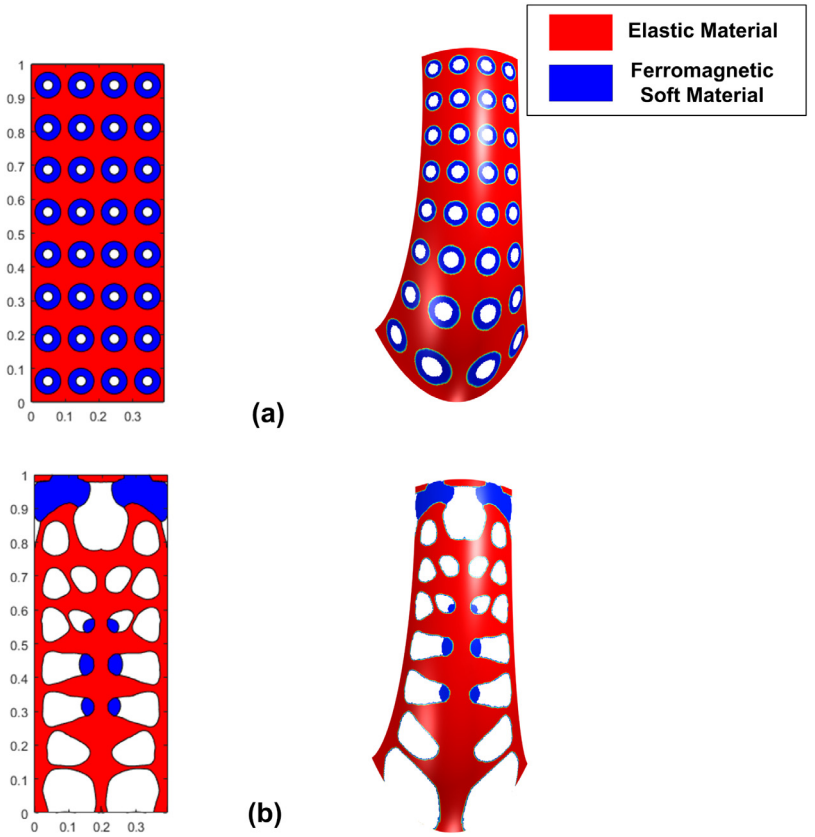

Fig. 22. The (a) initial and (b) final design of the flytrap soft active shell structure with two constituent materials. (For interpretation of the references to color in this figure legend, the reader is referred to the web version of this article.)

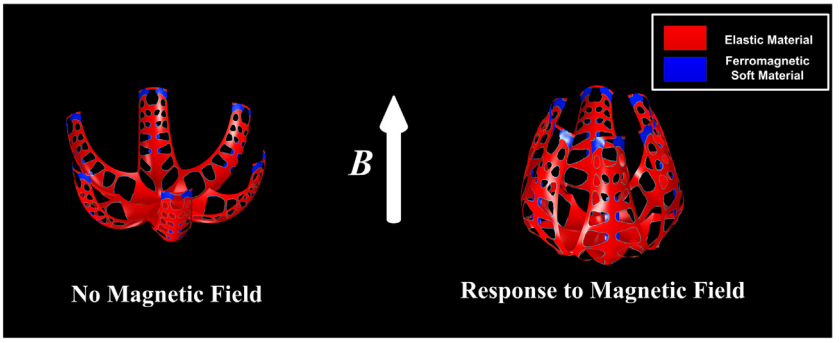

Fig. 23. Simulation of the grasping process of the multi-material flytrap soft active shell structure.

5. Numerical verification

5.1. STL generation of optimized conformal soft active structures

Before validating the performance of optimized results, STL models of optimized conformal ferromagnetic soft active structures are built. In this section, the framework for STL generation of the optimized conformal designs will be illustrated using the flytrap soft active shell structure, shown in Fig. 27. The algorithm of this framework is summarized in Algorithm 1. In the first step of Algorithm 1, a conformal mapping between a 3D triangle meshed

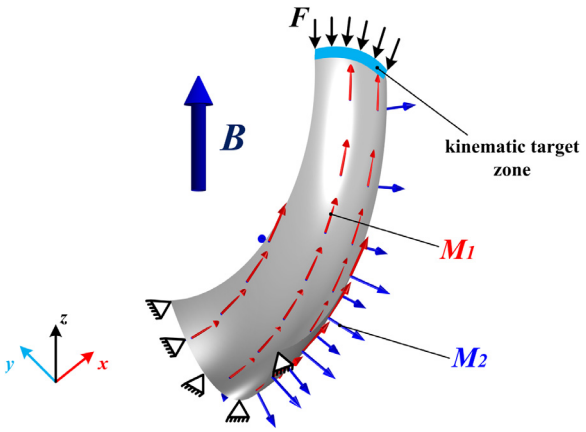

Fig. 24. Boundary condition of flytrap soft active shell structure with two actuating materials (only one finger). (For interpretation of the references to color in this figure legend, the reader is referred to the web version of this article.)

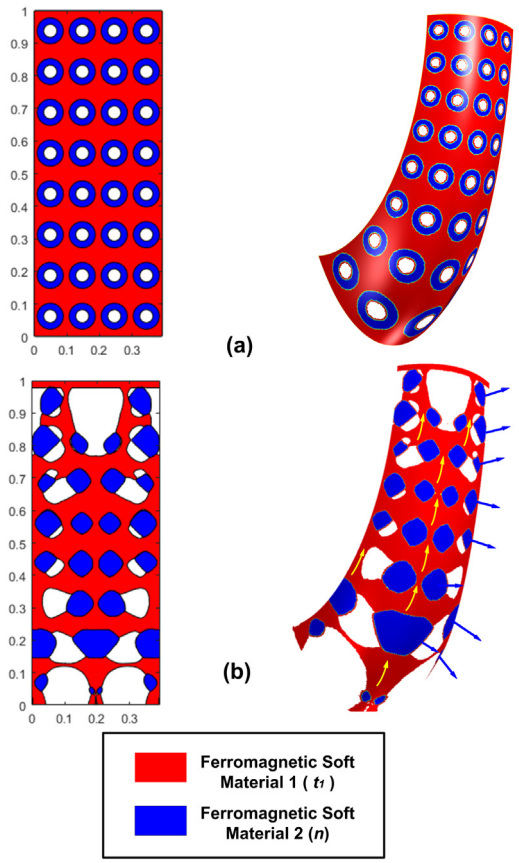

Fig. 25. The (a) initial and (b) final design of the flytrap soft active shell structure with two actuating materials. (For interpretation of the references to color in this figure legend, the reader is referred to the web version of this article.)

surface S_1, and a 2D triangle meshed rectangle Q_1 is computed. Therefore, the point-to-point relation between surface S_1 and rectangle Q_1 in the Euclidean space can be obtained. Based on the 2D optimized design represented by the level set function ϕ, a 2D STL file can be generated [74]. This 2D STL file can be re-meshed with triangle

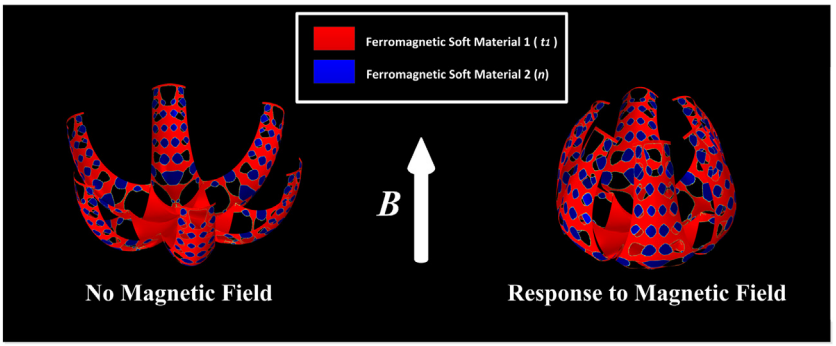

Fig. 26. Simulation of the grasping process of the flytrap soft active shell structure with two actuating materials.

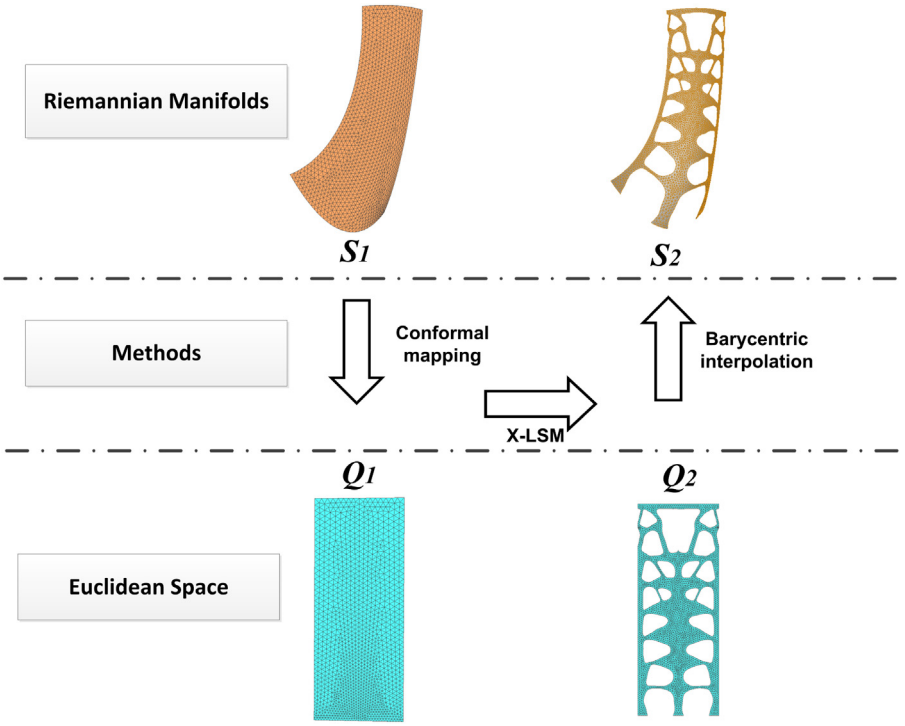

Fig. 27. The process of STL generation of optimized conformal soft active structures.

units, which is a 2D triangle meshed rectangle Q_2. Obviously, the boundaries of 2D rectangles Q_1 and Q_2 are in mutual coincidence. That is, any vertex on the 2D triangle meshed rectangle Q_2 is inside one of the triangles in rectangle Q_1. Hence, using the Barycentric interpolation method [75], we can calculate every vertex's Barycentric coordinates on the 2D triangle meshed rectangle Q_2. Consider a triangle that is defined by three vertices r_1, r_2 and r_3. A point r inside this triangle can be expressed as a unique convex combination of the three vertices as follows:

$$\begin{aligned} &r = \alpha r_1 + \beta r_2 + \gamma r_3, \\ &\alpha + \beta + \gamma = 1, \alpha, \beta, \gamma \geq 0, \end{aligned} \tag{33}$$

where α, β and γ indicate the Barycentric coordinates of the point r. Thus, the Barycentric coordinates α, β and γ can be calculated. Based on the point-to-point relation, we can find the vertices of v_1, v_2 and v_3 on the triangle meshed surface S_1, which are corresponding to the vertices r_1, r_2 and r_3 on 2D triangle meshed rectangle Q_1. Next,

Algorithm 1: STL Generation of Conformal Ferromagnetic Soft Active Structures

Input: A triangle meshed surface S_1 and a level set function ϕ representing the optimized design.
Output: STL of Optimized Conformal Ferromagnetic Soft Active Structures.
1:Given a triangle meshed surface S_1, compute a conformal mapping from S_1 to the 2D rectangle Q_1.
2:Generate the 2D triangle mesh rectangle Q_2 based on the obtained level set function ϕ representing the optimized design.
3:Using Barycentric interpolation method, calculate the corresponding 3D triangle mesh surface S_2 based on the triangle meshed surface S_1 and 2D triangle meshed rectangle Q_1.
4:Obtain the STL file of optimized shell structure.
5:Carry out some post-processing work including adding thickness, mirroring or arraying the designs to obtain STL of optimized conformal ferromagnetic soft active structures.

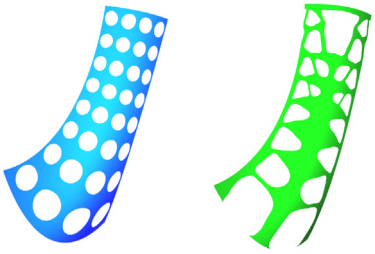

Fig. 28. STL model generation. (a) The initial design. (b) The optimized design.

the Cartesian coordinates of vertex v on the triangle meshed surface S_2 can be calculated as follows:

$$v = \alpha v_1 + \beta v_2 + \gamma v_3 \tag{34}$$

Having obtained the coordinate of every vertex v, we can form a surface S_2 with triangle meshes. In the last step, some necessary post-processing procedures (adding thickness, mirroring, or arraying et al.) can be done to obtain the STL file of optimized conformal designs.

5.2. Numerical verification

Based on the proposed Algorithm 1, the models of the optimized design and its corresponding initial design have been generated, as shown in Fig. 28. The purpose of this work is to design the ferromagnetic soft active structures that meet the requirements on kinematics and loading capacity. For conciseness, the verification work is detailed via the optimized flytrap soft active shell structure with single material. To validate the performance of the optimized design, the same boundary conditions are applied to the optimized flytrap petal, as shown in the previous Fig. 18. For the flytrap structure, the initial petal surface and the optimized petal surface are meshed with 31 236 and 20 218 triangular elements. For brevity, the Mises stress contour and displacement field simulated by COMSOL are provided only for the optimized flytrap soft active shell structure with single constituent material, as shown in Fig. 29.

As shown in Table 1, the strain energies of the initial and optimized designs were compared, and it turns out that the optimized designs yield lower strain energy when the interaction force is applied. Specifically, the mechanical benefit in terms of strain energy decreases by and 15.56% for the optimized flytrap soft active shell structure.

We also compared the deviation of the displacement from its target at 200 sampling points in the concerned area for kinematic performance (the blue areas shown in Fig. 18). The statistical deviations is listed in Table 2 for

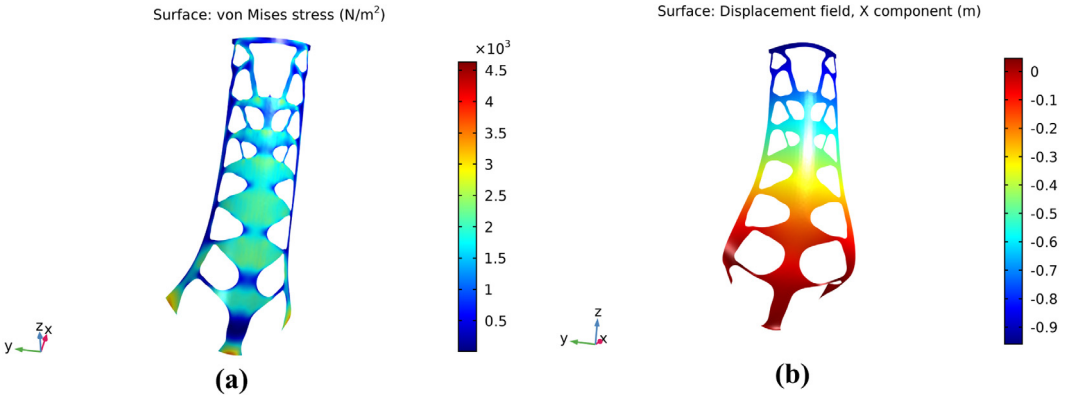

Fig. 29. Simulation results of the optimized flytrap soft active shell structure using COMSOL. (a) Mises stress contour. (b) Displacement field.

Table 1
Comparison of the total strain energy in the initial and optimized designs under the same loading condition.

	$SE_{initial}$	$SE_{optimal}$	$\frac{SE_{initial}-SE_{optimal}}{SE_{initial}} \times 100\%$
Flytrap soft active shell structure	14 781	12 481	15.56%

Table 2
Comparison of the displacement deviation in the flytrap soft active shell structure.

	Maximum deviation (m)	Minimum deviation (m)	Average deviation (m)
Initial design	0.3782	0.2826	0.3293
Optimal design	0.0493	0.0104	0.0311

the flytrap soft active shell structure. The comparison results show that the deviation from the target displacement decreases dramatically after optimization, demonstrating the satisfaction with the kinematic requirement.

In summary, the numerical verification results indicate the effectiveness of the proposed conformal topology optimization method for designing conforming ferromagnetic soft active structures on the manifolds.

6. Functional 3D printing

6.1. Patterning 3D magnetization

In this study, the optimized ferromagnetic soft active structures were printed using the magnetic-field-assisted mask-image-projection stereolithography (mMIP-SL) process. Fig. 30 shows the physical printing apparatus of mMIP-SL. The slurry in the tank for 3D printing was prepared by mixing magnetized neodymium-iron-boron (NdFeB) particles with flexible UV resin. The mass ratio between the NdFeB hard-magnetic particles (MQFP, 20441-089) and the UV resin (Formlabs™, Elastic 50 A) was set at 2:3. During the printing process, these NdFeB particles with an average diameter of 5 μm could be reoriented precisely in any spatial direction by two sets of electromagnetic coil systems. One can generate a magnetic field along the *Z*-axis, while the other, mounted on a turntable, can be dynamically rotated to generate a magnetic field within the *XY* plane. Both sets of electromagnetic coil systems can provide a uniform magnetic field of up to 60 mT. It usually takes 3 s for the NdFeB particles to be reoriented along the desired direction under the aligning magnetic field. After particle reorientation, an integrated digital light processing (DLP) projector emitted a mask pattern with 405 nm ultraviolet (UV) light to cure the selected sub-regions for 20 s. The solidified resin froze the particles within those regions in the slurry. Thereafter, the remaining magnetic particles in the unsolidified regions can be reoriented to another direction, following the projection of the second associated UV pattern. This automated procedure was repeated until all the sub-regions in the whole layer were cured. Then the building platform, where the cured layer was attached, was lifted by the

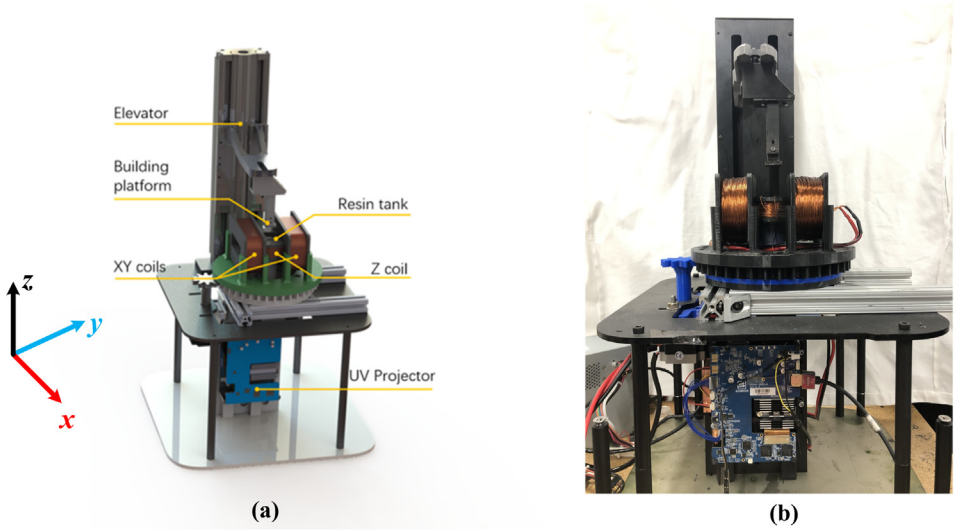

Fig. 30. Physical printing apparatus (a) schematic diagram of the setup for mMIP-SL. (b) image of the setup for mMIP-SL.

motorized elevator at 0.1 mm/s separation speed to prevent the sample from detaching from the building platform. Subsequently, the tank was refilled manually due to the high viscosity of the slurry under the selected weight ratio. When the tank was ready, the building platform was lowered to the position defined by a layer thickness of 100 μm, and the next layer was printed following the same procedures. The final 3D object could be obtained after repeating the procedure for all the layers.

6.2. Planar magnetically driven flytrap soft active structure

Grasping is among the most useful motions of soft robots. In this section, owing to the limitation of the current proposed 3D printing process, the planar magnetically driven 6-finger flytrap soft active structure is firstly fabricated to recast its grasping behaviors under the applied magnetic field. This printed structure with oriented magnetic particles is able to bend under the applied magnetic field and recover the original shape when the magnetic field is removed. The STL model used for printing is generated from the 2D optimized ferromagnetic flytrap result in Section 4.3. The petal with dimension of 19 mm × 7 mm × 0.6 mm fabricated by the mMIP-SL process is shown in Fig. 31(a).

Next, we studied the actuated behavior of a flytrap petal and demonstrated its shape transformation under the applied magnetic field. A permanent magnet was used for inducing the bending deformation and the applied magnetic field intensity is adjusted by controlling the distance between the magnet and the printed sample. As shown in Fig. 31(b), the left end of the petal is clamped and the free end is able to bend under the actuation of an upward applied magnetic field. The petal with length $L = 19$ m at the original position is illustrated by the gray line segment. The deformation of the petal is characterized by the position of the petal tip, namely the Cartesian coordinate $(\delta x, \delta y)$. Different positions of the petal tip were measured at a set of prescribed field strengths ranging from 0 to 60 mT. The result is vividly illustrated in Fig. 31(c). It can be found that starting from a horizontal position under no magnetic field, the petal tends to bend upward to enable the direction of the internal magnetization to be parallel with the external magnetic field. When the magnetic field goes stronger, the extent of actuated deformation becomes larger. The right free end almost reached a vertical position as the magnetic field are nearly 60 mT. For comparison, a corresponding FEM simulation was made to a petal with the same dimension as the printed sample. The boundary condition for the simulation kept exactly identical with the experiment. The Young's modulus of the Elastic 50 A is 1.7 MPa. However, owing to the lack of a vibrating sample magnetometer, the magnetic moment density (magnetization) cannot be measured and evaluated directly. Here, we assume the magnetization is $M = 8 \times 10^4$ A/m, which is same as that used in simulation during the optimization process. The simulated deflection of the petal tip under a set of magnetic field strengths ranging from 0 to 60 mT is given in Fig. 31(d). By

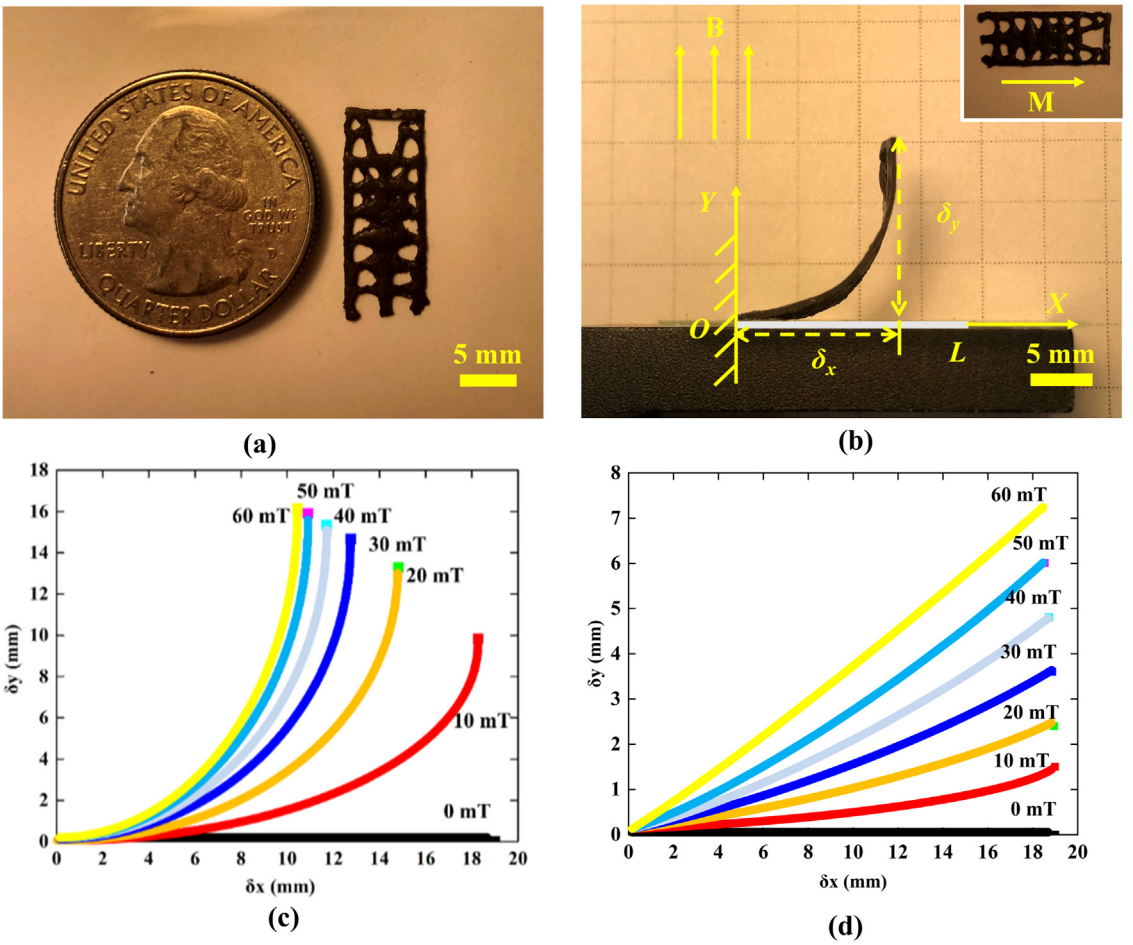

Fig. 31. (a) 3D printing sample of flytrap petal. (b) The position of the tip is characterized by a Cartesian coordinate (δx, δy). (c) Experiment: Deformed profiles of a flytrap petal under different magnetic field strengths $\boldsymbol{B}$=0, 10, 20, 30, 40, 50, 60 mT. (d) Simulation: Deformed profiles of flytrap petal under different magnetic field strengths $\boldsymbol{B}$ = 0, 10, 20, 30, 40, 50, 60 mT.

comparison, there are some disparities between the experiment and simulation results. For the simulation result, the deformation in the X direction has little change and the curvatures of the deformation configurations are relatively small. In addition, the deformation in the Y direction are smaller than the experiment result. This difference can be attributed to the different material models. For the soft rubbery material, it typically undergoes large and flexible deformations when subjected to a loading. Thus, the hyperelastic models are more suitable to characterize their nonlinear behaviors.

As shown in Fig. 32(a), a flower-like flytrap soft active structure is finally assembled by gluing six petals onto a hexagon flexible plate, which is made from the same material. Then we demonstrated the grasping behavior of the flytrap soft active structure under the applied magnetic field. All petals bend upward to present a half-closed shape under a 60 mT applied magnetic field, as presented in Fig. 32(b). In Fig. 32(c), the flytrap soft active structure is fully closed as the applied magnetic field increases to about 100 mT.

6.3. Magnetically driven gripper

In addition to 3D shape transformation, in-plane deformation can also be achieved by magnetic soft active structures. Fig. 33(a) shows a magnetically driven gripper(one finger) with the thickness of 2.0 mm fabricated by the mMIP-SL process. The STL model of this printed sample is generated from the optimized ferromagnetic

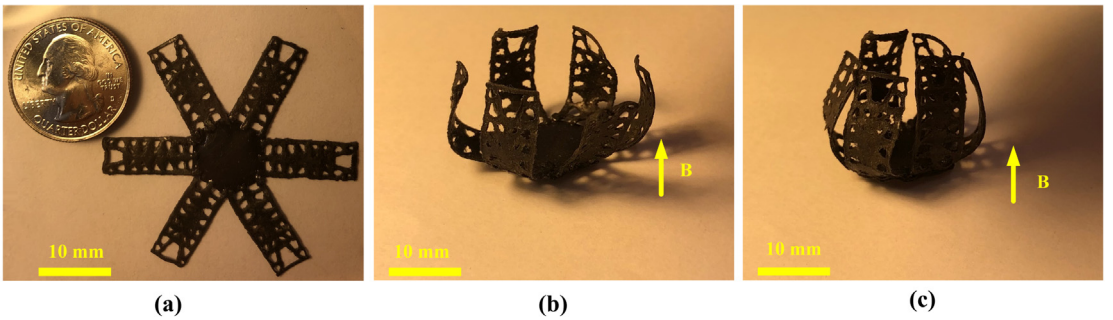

Fig. 32. Assembled 3D printing flytrap soft active structure and shape changes under applied magnetic field. (a) no magnetic field. (b) response to the magnetic field (intermediate deformed configuration). (c) response to the magnetic field (final deformed configuration).

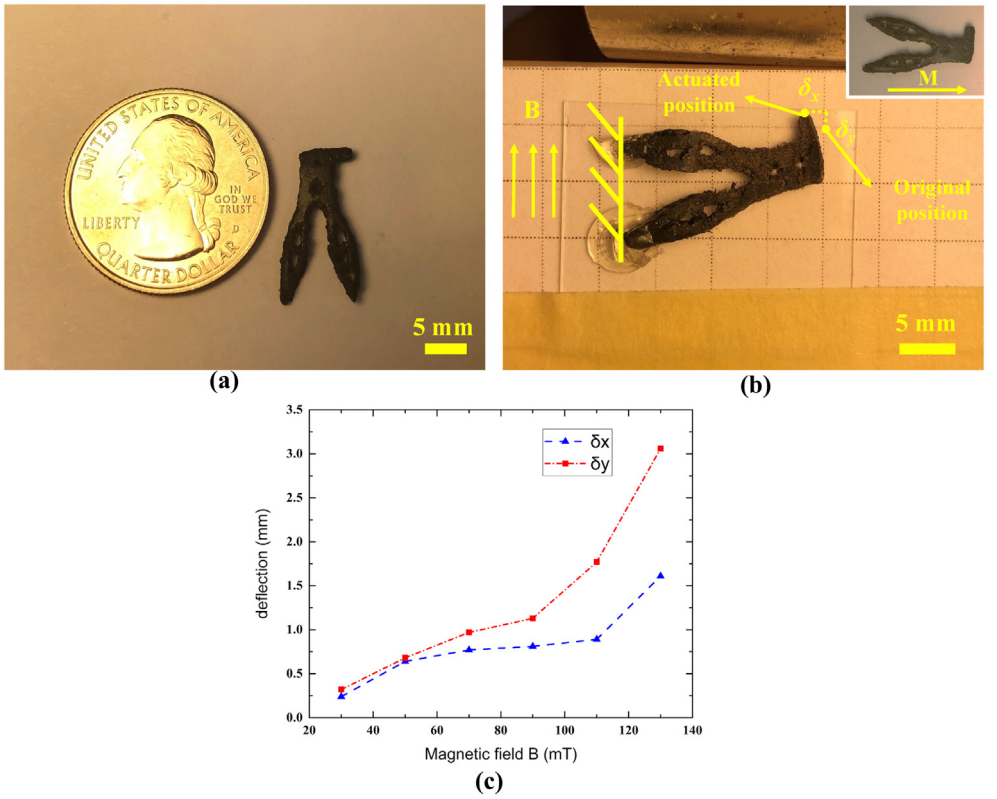

Fig. 33. (a) 3D printing sample of gripper(one finger). (b) The deflection of the gripper tip in response to magnetic field. (c) The deflection of the gripper tip under different magnetic field strengths $\boldsymbol{B}$ = 30, 50, 70, 90, 110, 130 mT.

gripper, which has been presented in [55]. As depicted in Fig. 33(b), a similar approach was adopted to study the stimulated behavior of the ferromagnetic gripper, within which the magnetization is pointing to the right. With the left end of the sample being clamped, the right free end is free to move under the actuation of the applied magnetic field. In detail, the gripper finger is liable to bend upward so that the inner magnetization has a tendency to be parallel with the external upward magnetic field. To measure the deformation, we recorded the deflection (δx and δy) of the gripper finger tip in response to various magnetic field strengths ranging from 30 to 130 mT, as shown in Fig. 33(c). It can be noticed that with the increasing of the magnetic field strengths, the deflection in X and Y direction becomes larger. Finally, we demonstrated the original configuration with no applied magnetic field and the bending configuration in response to a 200 mT magnetic field respectively, as illustrated in Fig. 34.

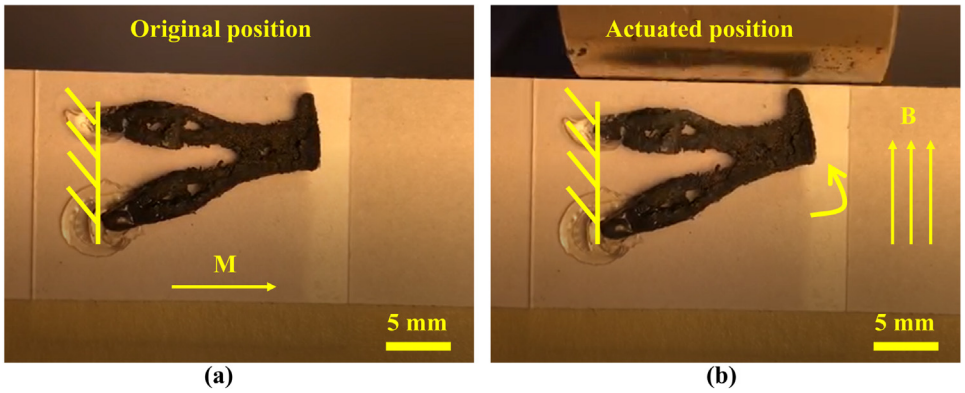

Fig. 34. 3D printing gripper (one finger) and shape changes under applied magnetic field. (a) Original configuration. (b) Deformed bending configuration.

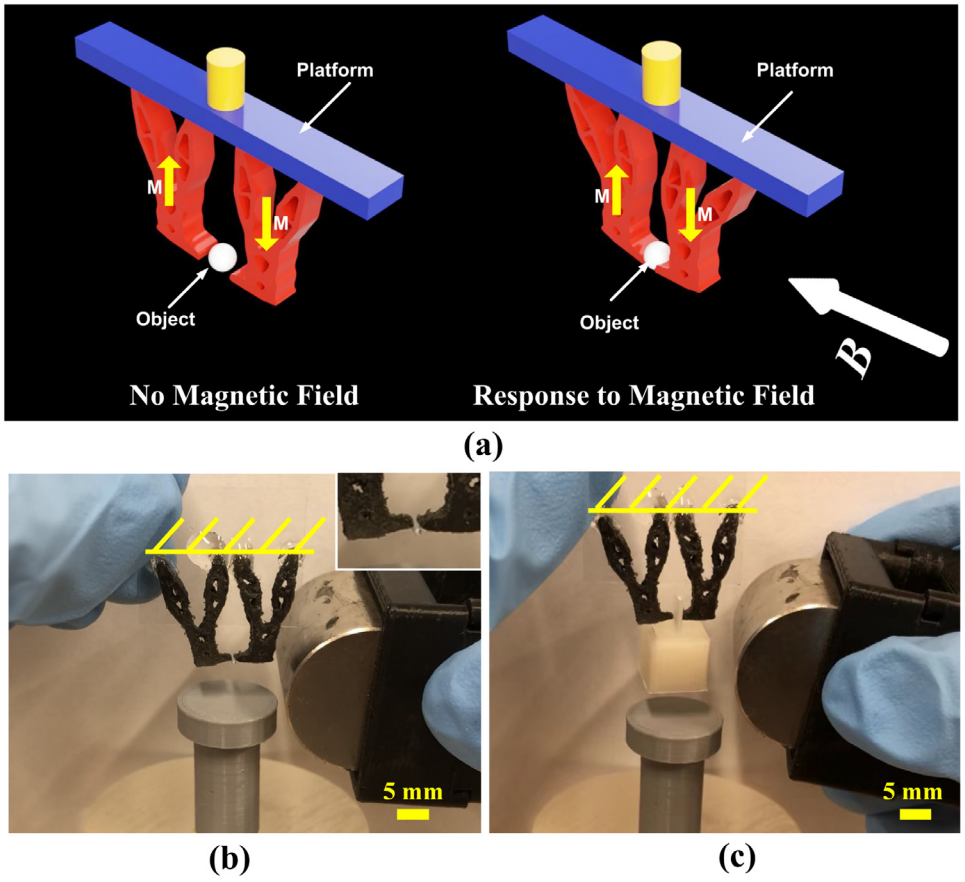

Fig. 35. Numerical verification and physical validation of the 2D gripper presented in [55]. (a) Simulation of grasping process. (b) Grasping a small rod by a pair of grippers with the opposite magnetization directions. (c) Grasping an object weighted 1.1 g by a pair of grippers with the opposite magnetization directions.

By utilizing this in-plane bending capability, another gripper with opposite magnetization orientation was printed out to form a set of grippers for small object grasping purposes. The weight of this pair of grippers is 0.36 g. An overview of the grasping object is given in Fig. 35(a), where two grippers with opposite magnetization direction are

positioned as mirror symmetric distribution and mounted on a platform [55]. One grasped object is a small rod with the diameter of 0.75 mm and length of 4 mm, which can be grasped and lifted successfully shown in Fig. 35(b). Another grasped object weighted 1.1 g, which is 3 times as heavy as the set of grippers. As shown in Fig. 35, two grippers bent towards the center to grasp the object under the applied magnetic field.

6.4. Discussion

In this paper, we mainly demonstrated the capability to obtain spatial orientations of the magnetic particles in planar structures with multiple layers. The fabrication of the curved thin-shell structures, however, could be a challenge using the current setup. This is because the cured flexible material was unable to maintain its shape very well under the large separation force when it was detached from the bottom of the tank and the large resistance when it reentered the highly viscous resin. In the future work, we are planning to fabricate the curved thin-shell ferromagnetic soft active structures using the molding method. The magnetic slurry is poured into a pre-printed 3D cavity, and the whole structure can be cured after the magnetic particles are reoriented by an external magnetic field.

In addition, the maximum size of samples printed by the magnetic-field-assisted mask-image-projection stereolithography setup is approximate 20 mm $\times$ 20 mm. Therefore, some manual assembly work is required during the fabrication of certain large objects. Another limitation is the warpage and curling are liable to generate in the printed planar structures. The reason for this issue is the opacity of the magnetic particles, making the bottom side receive relatively more UV light than the upper side. This brings additional cross-linking on the bottom of each layer and thus extra shrinkage, which finally causes the planar structure to curl when it is released from the building platform.

7. Conclusions

In this paper, an effective level set-based multiphysics topology optimization method was developed for ferromagnetic soft active structures design. The reconciled level set (RLS) method was used especially for designing the multi-material ferromagnetic soft active structures and the ferromagnetic soft active structures in the form of manifolds was designed by taking advantage of the extended level set methods and the conformal geometry theory. The magnetic field and solid mechanics field are coupled in the ferromagnetic soft active structure design models. A magnetic body force is adopted to control the deformation of the ferromagnetic soft active structures. At the current stage, we simplify the problem by assuming the material is linear elastic when implementing the linear finite element analysis, although the soft material presents certain hyperelasticity. The design problem is recast as a balance of the kinematic performance and load-carrying capability. Five numerical examples are carried out to testify the proposed method. The STL files of topology optimization results in manifolds were subsequently generated using the Barycentric interpolation and conformal geometry theory. The numerical verification results show that the optimized design meets the kinematics requirement to reach the displacement target. Moreover, the stiffness of the optimized designs increases 15.56% compared with its initial design, indicating that the optimized design have relatively better load carrying capability. The improved loading carrying and kinematic performances of the optimized designs demonstrate the validity of the proposed methodology. Finally, the optimized magnetically driven flytrap and gripper were printed out with the magnetic-field-assisted mask-image-projection stereolithography (mMIP-SL) process. The grasping behaviors of the printed samples were stimulated by the applied magnetic field. The measurement and analysis were conducted to the deformation of the samples in response to different magnetic field strengths.

While the preliminary results are encouraging, there is a lot of room for improvement in the future studies. One of our efforts will be to better incorporate the material and geometry nonlinearity into the topology optimization of ferromagnetic soft active structures in order to accurately model their mechanical behaviors. Besides, we plan to use mMIP-SL process to print multi-material ferromagnetic soft active structures subsequently. In addition, the curved thin-shell ferromagnetic soft active structures will be fabricated by adding sufficient supports to the STL model or using the previously mentioned molding process. Moreover, we plan to set the magnetization orientation as a variable to conduct the multi-material topology optimization of the ferromagnetic soft active structures in future work.

Declaration of competing interest

The authors declare that they have no known competing financial interests or personal relationships that could have appeared to influence the work reported in this paper.

Acknowledgments

This work is supported by National Science Foundation (NSF), USA (CMMI-1462270, CMMI-1762287), the Ford University Research Program (URP), USA (Award No. 2017-9198R), and the start-up fund from the State University of New York at Stony Brook, USA. The authors would like to sincerely thank Prof. Xuanhe Zhao at MIT for the insightful discussions and also for providing the Abaqus code for ferromagnetic material modeling.

References

[1] M. Wehner, R.L. Truby, D.J. Fitzgerald, B. Mosadegh, G.M. Whitesides, J.A. Lewis, R.J. Wood, An integrated design and fabrication strategy for entirely soft, autonomous robots, Nature 536 (7617) (2016) 451.
[2] S. Kim, C. Laschi, B. Trimmer, Soft robotics: a bioinspired evolution in robotics, Trends Biotechnol. 31 (5) (2013) 287–294.
[3] M. Zarek, M. Layani, I. Cooperstein, E. Sachyani, D. Cohn, S. Magdassi, 3D printing of shape memory polymers for flexible electronic devices, Adv. Mater. 28 (22) (2016) 4449–4454.
[4] J.A. Fan, W.-H. Yeo, Y. Su, Y. Hattori, W. Lee, S.-Y. Jung, Y. Zhang, Z. Liu, H. Cheng, L. Falgout, et al., Fractal design concepts for stretchable electronics, Nature Commun. 5 (2014) 3266.
[5] X. Zhao, J. Kim, C.A. Cezar, N. Huebsch, K. Lee, K. Bouhadir, D.J. Mooney, Active scaffolds for on-demand drug and cell delivery, Proc. Natl. Acad. Sci. 108 (1) (2011) 67–72.
[6] M. Cianchetti, C. Laschi, A. Menciassi, P. Dario, Biomedical applications of soft robotics, Nat. Rev. Mater. (2018) 1.
[7] K. Asaka, H. Okuzaki, Soft Actuators: Materials, Modeling, Applications, and Future Perspectives, Springer, 2014.
[8] Y. Kim, H. Yuk, R. Zhao, S.A. Chester, X. Zhao, Printing ferromagnetic domains for untethered fast-transforming soft materials, Nature 558 (7709) (2018) 274.
[9] W. Zhang, S. Ahmed, S. Masters, Z. Ounaies, M. Frecker, Finite element analysis of electroactive polymer and magnetoactive elastomer based actuation for origami-inspired folding, in: ASME 2016 Conference on Smart Materials, Adaptive Structures and Intelligent Systems, American Society of Mechanical Engineers, 2016, V001T01A001.
[10] T. Brunet, A. Merlin, B. Mascaro, K. Zimny, J. Leng, O. Poncelet, C. Aristégui, O. Mondain-Monval, Soft 3D acoustic metamaterial with negative index, Nature Mater. 14 (4) (2015) 384.
[11] D.G. Grier, A revolution in optical manipulation, Nature 424 (6950) (2003) 810.
[12] E.J. Peterman, F. Gittes, C.F. Schmidt, Laser-induced heating in optical traps, Biophys. J. 84 (2) (2003) 1308–1316.
[13] R.M. Erb, J.J. Martin, R. Soheilian, C. Pan, J.R. Barber, Actuating soft matter with magnetic torque, Adv. Funct. Mater. 26 (22) (2016) 3859–3880.
[14] T. Grahl, H. Märkl, Killing of microorganisms by pulsed electric fields, Appl. Microbiol. Biotechnol. 45 (1–2) (1996) 148–157.
[15] A. Ranzoni, X.J. Janssen, M. Ovsyanko, L.J. van IJzendoorn, M.W. Prins, Magnetically controlled rotation and torque of uniaxial microactuators for lab-on-a-chip applications, Lab Chip 10 (2) (2010) 179–188.
[16] R.M. Erb, N.J. Jenness, R.L. Clark, B.B. Yellen, Towards holonomic control of Janus particles in optomagnetic traps, Adv. Mater. 21 (47) (2009) 4825–4829.
[17] T. Xu, J. Zhang, M. Salehizadeh, O. Onaizah, E. Diller, Millimeter-scale flexible robots with programmable three-dimensional magnetization and motions, Science Robotics 4 (29) (2019) eaav4494.
[18] S. Wu, Q. Ze, R. Zhang, N. Hu, Y. Cheng, F. Yang, R. Zhao, Symmetry-breaking actuation mechanism for soft robotics and active metamaterials, ACS Appl. Mater. Interfaces 11 (44) (2019) 41649–41658.
[19] R. Zhao, Y. Kim, S.A. Chester, P. Sharma, X. Zhao, Mechanics of hard-magnetic soft materials, J. Mech. Phys. Solids 124 (2019) 244–263.
[20] L. Wang, Y. Kim, C.F. Guo, X. Zhao, Hard-magnetic elastica, J. Mech. Phys. Solids (2020) 104045.
[21] G.Z. Lum, Z. Ye, X. Dong, H. Marvi, O. Erin, W. Hu, M. Sitti, Shape-programmable magnetic soft matter, Proc. Natl. Acad. Sci. 113 (41) (2016) E6007–E6015.
[22] E. Diller, J. Zhuang, G. Zhan Lum, M.R. Edwards, M. Sitti, Continuously distributed magnetization profile for millimeter-scale elastomeric undulatory swimming, Appl. Phys. Lett. 104 (17) (2014) 174101.
[23] C. Zhang, X. Li, L. Jiang, D. Tang, X. Han, P. Zhao, J. Fu, Q. Zhou, Y. Chen, 3D printing of functional magnetic materials: From design to applications." Advanced functional materials, in: Advanced Functional Materials, Vol. 5, Wiley Online Library, 2021, V010T10A012.
[24] Q. Ye, Y. Guo, S. Chen, N. Lei, X.D. Gu, Topology optimization of conformal structures on manifolds using extended level set methods (X-LSM) and conformal geometry theory, Comput. Methods Appl. Mech. Engrg. 344 (2019) 164–185.
[25] H.C. Ko, M.P. Stoykovich, J. Song, V. Malyarchuk, W.M. Choi, C.-J. Yu, J.B. Geddes Iii, J. Xiao, S. Wang, Y. Huang, et al., A hemispherical electronic eye camera based on compressible silicon optoelectronics, Nature 454 (7205) (2008) 748.
[26] H.C. Ko, G. Shin, S. Wang, M.P. Stoykovich, J.W. Lee, D.-H. Kim, J.S. Ha, Y. Huang, K.-C. Hwang, J.A. Rogers, Curvilinear electronics formed using silicon membrane circuits and elastomeric transfer elements, Small 5 (23) (2009) 2703–2709.

[27] J.-H. Zhu, W.-H. Zhang, L. Xia, Topology optimization in aircraft and aerospace structures design, Arch. Comput. Methods Eng. 23 (4) (2016) 595–622.
[28] J.-w. Tian, K. Bu, J.-h. Song, G.-l. Tian, F. Qiu, D.-q. Zhao, Z.-l. Jin, Y. Li, Optimization of investment casting process parameters to reduce warpage of turbine blade platform in DD6 alloy, China Foundry 14 (6) (2017) 469–477.
[29] R.-s. Jiang, D.-h. Zhang, K. Bu, W.-h. Wang, J.-w. Tian, A deformation compensation method for wax pattern die of turbine blade, Int. J. Adv. Manuf. Technol. 88 (9–12) (2017) 3195–3203.
[30] F. Chen, M.Y. Wang, Design optimization of soft robots: A review of the state of the art, IEEE Robot. Autom. Mag. (2020).
[31] M. Bendsøe, O. Sigmund, Theory, methods and applications, in: Topology Optimization, Springer, Berlin, 2003.
[32] O. Sigmund, K. Maute, Topology optimization approaches, Struct. Multidiscip. Optim. 48 (6) (2013) 1031–1055.
[33] N.P. van Dijk, K. Maute, M. Langelaar, F. Van Keulen, Level-set methods for structural topology optimization: a review, Struct. Multidiscip. Optim. 48 (3) (2013) 437–472.
[34] X. Xu, Y. Wu, L. Zuo, S. Chen, Topology optimization of multimaterial thermoelectric structures, J. Mech. Des. 143 (2021) 011705.
[35] X. Xu, Y. Wu, L. Zuo, S. Chen, Multimaterial topology optimization of thermoelectric generators, in: International Design Engineering Technical Conferences and Computers and Information in Engineering Conference, American Society of Mechanical Engineers, 2019, V02AT03A064.
[36] R. Behrou, R. Lotfi, J.V. Carstensen, F. Ferrari, J.K. Guest, Revisiting element removal for density-based structural topology optimization with reintroduction by Heaviside projection, Comput. Methods Appl. Mech. Engrg. 380 (2021) 113799.
[37] K. Wu, O. Sigmund, J. Du, Design of metamaterial mechanisms using robust topology optimization and variable linking scheme, Struct. Multidiscip. Optim. 63 (4) (2021) 1975–1988.
[38] M.J. Geiss, N. Boddeti, O. Weeger, K. Maute, M.L. Dunn, Combined level-set-XFEM-density topology optimization of four-dimensional printed structures undergoing large deformation, J. Mech. Des. 141 (5) (2019) 051405.
[39] F. Chen, W. Xu, H. Zhang, Y. Wang, J. Cao, M.Y. Wang, H. Ren, J. Zhu, Y. Zhang, Topology optimized design, fabrication, and characterization of a soft cable-driven gripper, IEEE Robot. Autom. Lett. 3 (3) (2018) 2463–2470.
[40] K. Furuta, K. Izui, K. Yaji, T. Yamada, S. Nishiwaki, Level set-based topology optimization for the design of a peltier effect thermoelectric actuator, Struct. Multidiscip. Optim. 55 (5) (2017) 1671–1683.
[41] M.Y. Wang, S. Chen, X. Wang, Y. Mei, Design of multimaterial compliant mechanisms using level-set methods, J. Mech. Des. 127 (5) (2005) 941–956.
[42] S.-i. Park, S. Min, Design of magnetic actuator with nonlinear ferromagnetic materials using level-set based topology optimization, IEEE Trans. Magn. 46 (2) (2010) 618–621.
[43] S.-i. Park, S. Min, S. Yamasaki, S. Nishiwaki, J. Yoo, Magnetic actuator design using level set based topology optimization, IEEE Trans. Magn. 44 (11) (2008) 4037–4040.
[44] N. Ryu, S. Lim, S. Min, K. Izui, S. Nishiwaki, Multi-objective optimization of magnetic actuator design using adaptive weight determination scheme, IEEE Trans. Magn. 53 (6) (2017) 1–4.
[45] S.-I. Park, S. Min, Magnetic actuator design for maximizing force using level set based topology optimization, IEEE Trans. Magn. 45 (5) (2009) 2336–2339.
[46] Y. Li, L. Liu, S. Yang, Z. Ren, Y. Ma, A multi-objective topology optimization methodology and its application to electromagnetic actuator designs, IEEE Trans. Magn. 56 (2) (2020) 1–4.
[47] P. Liu, L. Shi, Z. Kang, Multi-material structural topology optimization considering material interfacial stress constraints, Comput. Methods Appl. Mech. Engrg. 363 (2020) 112887.
[48] X. Guo, W. Zhang, W. Zhong, Stress-related topology optimization of continuum structures involving multi-phase materials, Comput. Methods Appl. Mech. Engrg. 268 (2014) 632–655.
[49] H. Kazemi, A. Vaziri, J.A. Norato, Multi-material topology optimization of lattice structures using geometry projection, Comput. Methods Appl. Mech. Engrg. 363 (2020) 112895.
[50] M.Y. Wang, X. Wang, "Color" level sets: a multi-phase method for structural topology optimization with multiple materials, Comput. Methods Appl. Mech. Engrg. 193 (6–8) (2004) 469–496.
[51] H. Zhang, A.S. Kumar, F. Chen, J.Y. Fuh, M.Y. Wang, Topology optimized multimaterial soft fingers for applications on grippers, rehabilitation, and artificial hands, IEEE/ASME Trans. Mechatronics 24 (1) (2018) 120–131.
[52] H. Zhang, A.S. Kumar, J.Y.H. Fuh, M.Y. Wang, Investigation on developing a topology optimized and 3D printable multimaterial soft gripper, in: 2018 IEEE 14th International Conference on Control and Automation (ICCA), IEEE, 2018, pp. 692–697.
[53] J. Hiller, H. Lipson, Automatic design and manufacture of soft robots, IEEE Trans. Robot. 28 (2) (2011) 457–466.
[54] S. Sundaram, M. Skouras, D.S. Kim, L. van den Heuvel, W. Matusik, Topology optimization and 3D printing of multimaterial magnetic actuators and displays, Sci. Adv. 5 (7) (2019) eaaw1160.
[55] J. Tian, X. Zhao, X.D. Gu, S. Chen, Designing ferromagnetic soft robots (FerroSoRo) with level-set-based multiphysics topology optimization, in: 2020 IEEE International Conference on Robotics and Automation (ICRA), IEEE, 2020, pp. 10067–10074.
[56] J. Tian, X. Zhao, X.D. Gu, S. Chen, Designing conformal ferromagnetic soft actuators using extended level set methods (X-LSM), in: International Design Engineering Technical Conferences and Computers and Information in Engineering Conference, Vol. 83990, American Society of Mechanical Engineers, 2020, V010T10A012.
[57] H. Ghiasi, K. Fayazbakhsh, D. Pasini, L. Lessard, Optimum stacking sequence design of composite materials Part II: Variable stiffness design, Compos. Struct. 93 (1) (2010) 1–13.
[58] N. Boddeti, Y. Tang, K. Maute, D.W. Rosen, M.L. Dunn, Optimal design and manufacture of variable stiffness laminated continuous fiber reinforced composites, Sci. Rep. 10 (1) (2020) 1–15.
[59] Y. Tian, S. Pu, T. Shi, Q. Xia, A parametric divergence-free vector field method for the optimization of composite structures with curvilinear fibers, Comput. Methods Appl. Mech. Engrg. 373 (2021) 113574.

[60] J.D. Deaton, R.V. Grandhi, A survey of structural and multidisciplinary continuum topology optimization: post 2000, Struct. Multidiscip. Optim. 49 (1) (2014) 1–38.
[61] G. Allaire, F. Jouve, A.-M. Toader, Structural optimization using sensitivity analysis and a level-set method, J. Comput. Phys. 194 (1) (2004) 363–393.
[62] F. Chen, Y. Wang, M.Y. Wang, Y. Zhang, Topology optimization of hyperelastic structures using a level set method, J. Comput. Phys. 351 (2017) 437–454.
[63] X. Gu, Y. Wang, T.F. Chan, P.M. Thompson, S.-T. Yau, Genus zero surface conformal mapping and its application to brain surface mapping, IEEE Trans. Med. Imaging 23 (8) (2004) 949–958.
[64] L.M. Lui, X. Gu, T.F. Chan, S.-T. Yau, et al., Variational method on riemann surfaces using conformal parameterization and its applications to image processing, Methods Appl. Anal. 15 (4) (2008) 513–538.
[65] G.P. Choi, Y. Chen, L.M. Lui, B. Chiu, Conformal mapping of carotid vessel wall and plaque thickness measured from 3D ultrasound images, Med. Biol. Eng. Comput. 55 (12) (2017) 2183–2195.
[66] D.X. Gu, W. Zeng, L.M. Lui, F. Luo, S.-T. Yau, Recent development of computational conformal geometry, in: Fifth International Congress of Chinese Mathematicians. Part, Vol. 1, 2012, pp. 515–560.
[67] S. Chen, S. Gonella, W. Chen, W.K. Liu, A level set approach for optimal design of smart energy harvesters, Comput. Methods Appl. Mech. Engrg. 199 (37–40) (2010) 2532–2543.
[68] P. Vogiatzis, S. Chen, X. Wang, T. Li, L. Wang, Topology optimization of multi-material negative Poisson's ratio metamaterials using a reconciled level set method, Comput. Aided Des. 83 (2017) 15–32.
[69] L. Jiang, X. Gu, S. Chen, Generative design of bionic structures via concurrent multiscale topology optimization & conformal geometry method, J. Mech. Des. (2020) 1–29.
[70] C. Wang, X. Qian, A density gradient approach to topology optimization under design-dependent boundary loading, J. Comput. Phys. 411 (2020) 109398.
[71] A. Neofytou, R. Picelli, T.-H. Huang, J.-S. Chen, H.A. Kim, Level set topology optimization for design-dependent pressure loads using the reproducing kernel particle method, Struct. Multidiscip. Optim. 61 (5) (2020) 1805–1820.
[72] T. Zegard, G.H. Paulino, Bridging topology optimization and additive manufacturing, Struct. Multidiscip. Optim. 53 (1) (2016) 175–192.
[73] K. Liu, A. Tovar, An efficient 3D topology optimization code written in Matlab, Struct. Multidiscip. Optim. 50 (6) (2014) 1175–1196.
[74] P. Vogiatzis, S. Chen, C. Zhou, An open source framework for integrated additive manufacturing and level-set-based topology optimization, J. Comput. Inf. Sci. Eng. 17 (4) (2017).
[75] P. Vogiatzis, M. Ma, S. Chen, X.D. Gu, Computational design and additive manufacturing of periodic conformal metasurfaces by synthesizing topology optimization with conformal mapping, Comput. Methods Appl. Mech. Engrg. 328 (2018) 477–497.
[76] P. Saxena, On the general governing equations of electromagnetic acoustic transducers, Arch. Mech. Eng. 60 (2) (2013) 231–246.
[77] G. Bertotti, Hysteresis in Magnetism: For Physicists, Materials Scientists, and Engineers, Gulf Professional Publishing, 1998.
[78] T. Jung, J. Lee, J. Lee, Design and fabrication of magnetic system using multi-material topology optimization, IEEE Access 9 (2021) 8649–8658.
[79] J. Tian, X.D. Gu, S. Chen, Multi-material topology optimization of ferromagnetic soft robots using reconciled level set method, in: International Design Engineering Technical Conferences and Computers and Information in Engineering Conference, American Society of Mechanical Engineers, 2021, V08BT08A014.
[80] J. Liu, A.T. Gaynor, S. Chen, Z. Kang, K. Suresh, A. Takezawa, L. Li, J. Kato, J. Tang, C.C. Wang, et al., Current and future trends in topology optimization for additive manufacturing, Struct. Multidiscip. Optim. 57 (6) (2018) 2457–2483.
[81] B. Merriman, J.K. Bence, S.J. Osher, Motion of multiple junctions: A level set approach, J. Comput. Phys. 112 (2) (1994) 334–363.
[82] X. Zhang, J.-S. Chen, S. Osher, A multiple level set method for modeling grain boundary evolution of polycrystalline materials, Interact. Multiscale Mech. 1 (2) (2008) 178–191.
[83] Q. Ye, Y. Guo, S. Chen, X.D. Gu, N. Lei, Topology optimization of conformal structures using extended level set methods and conformal geometry theory, in: ASME 2018 International Design Engineering Technical Conferences and Computers and Information in Engineering Conference, American Society of Mechanical Engineers Digital Collection, 2018.
[84] X.D. Gu, S.-T. Yau, Computational Conformal Geometry, International Press, Somerville, MA, 2008.
[85] G. Allaire, F. Jouve, Optimal design of micro-mechanisms by the homogenization method, Rev. Eur. Elém. 11 (2–4) (2002) 405–416.
[86] O. Sigmund, On the design of compliant mechanisms using topology optimization, J. Struct. Mech. 25 (4) (1997) 493–524.
[87] K.K. Choi, N.-H. Kim, Structural Sensitivity Analysis and Optimization 1: Linear Systems, Springer Science & Business Media, 2006.
[88] M.Y. Wang, X. Wang, D. Guo, A level set method for structural topology optimization, Comput. Methods Appl. Mech. Engrg. 192 (1–2) (2003) 227–246.
[89] X. Xu, S. Chen, X.D. Gu, M.Y. Wang, Conformal topology optimization of heat conduction problems on manifolds using an extended level set method (x-lsm), in: ASME 2021 International Design Engineering Technical Conferences and Computers and Information in Engineering Conference, American Society of Mechanical Engineers Digital Collection, 2021.